

Alma Mater Studiorum Università di Bologna  
Archivio istituzionale della ricerca

Ligand-Mediated Control of the Surface Oxidation States of Copper Nanoparticles Produced by Laser Ablation

This is the final peer-reviewed author's accepted manuscript (postprint) of the following publication:

*Published Version:*

Mulder A.J., Tilbury R.D., Werrett M.V., Wright P.J., Patel P., Becker T., et al. (2023). Ligand-Mediated Control of the Surface Oxidation States of Copper Nanoparticles Produced by Laser Ablation. *LANGMUIR*, 39(14), 5156-5168 [10.1021/acs.langmuir.3c00225].

*Availability:*

This version is available at: <https://hdl.handle.net/11585/927573> since: 2023-11-08

*Published:*

DOI: <http://doi.org/10.1021/acs.langmuir.3c00225>

*Terms of use:*

Some rights reserved. The terms and conditions for the reuse of this version of the manuscript are specified in the publishing policy. For all terms of use and more information see the publisher's website.

This item was downloaded from IRIS Università di Bologna (<https://cris.unibo.it/>).  
When citing, please refer to the published version.

(Article begins on next page)

This is the final peer-reviewed accepted manuscript of:

**Ligand-mediated control of the surface oxidation states of copper nanoparticles produced by laser ablation**

Mulder, Ashley J.; Tilbury, Rhys D.; Werrett, Melissa V.; Wright, Phillip J.; Patel, Payal, Becker, Thomas; Jones, Franca; Stagni, Stefano; Jia, Guohua; Massi, Massimiliano; Buntine, Mark A. *Langmuir* (2023), 39, 5156-68.

DOI: 10.1021/acs.langmuir.3c00225

The final published version is available online at: <https://pubs-acsc-org.ezproxy.unibo.it/doi/10.1021/acs.langmuir.3c00225>

Terms of use:

Some rights reserved. The terms and conditions for the reuse of this version of the manuscript are specified in the publishing policy. For all terms of use and more information see the publisher's website.

# Ligand-mediated control of the surface oxidation states of copper nanoparticles produced by laser ablation

*Ashley J. Mulder,<sup>†</sup> Rhys D. Tilbury,<sup>†</sup> Melissa V. Werrett,<sup>†</sup> Phillip J. Wright,<sup>†</sup> Payal Patel,<sup>†,§</sup> Thomas Becker,<sup>†</sup> Franca Jones,<sup>†</sup> Stefano Stagni,<sup>‡</sup> Guohua Jia,<sup>†</sup> Massimiliano Massi<sup>†</sup> and Mark A. Buntine<sup>\*,†</sup>*

<sup>†</sup> Department of Chemistry, Curtin University, GPO Box U1987 Perth, WA 6845 Australia

<sup>§</sup> School of Chemistry, University of Southampton, SO17 1BJ, United Kingdom

<sup>‡</sup> Department of Industrial Chemistry “Toso Montanari”, University of Bologna, viale del Risorgimento 4, Bologna 40136 Italy

\* Corresponding author

Email: [m.buntine@curtin.edu.au](mailto:m.buntine@curtin.edu.au)

Running title: Ligand-mediated control of copper nanoparticle surface oxidation

Submitted to: Langmuir (Revised submission)

## **Abstract**

We report on studies that demonstrate how the chemical composition of the surface of copper nanoparticles (CuNPs) – in terms of percentage copper(I/II) oxides – can be varied by the presence of N-donor ligands during their formation via laser ablation. Changing the chemical composition thus allows systematic tuning of the Surface Plasmon Resonance (SPR) transition. The trialed ligands include pyridines, tetrazoles and alkylated tetrazoles. CuNPs formed in the presence of pyridines and alkylated tetrazoles exhibit a SPR transition only slightly blue shifted with respect to CuNPs formed in the absence of any ligand. On the other hand, the presence of tetrazoles results in CuNPs characterized by a significant blue shift of the order of 50-70 nm. By comparing these data also with the SPR of CuNPs formed in the presence of carboxylic acids and hydrazine, this work demonstrates that the blue shift in the SPR is due to tetrazolate anions providing a reducing environment to the nascent CuNPs, thus preventing the formation of copper (II) oxides. This conclusion is further supported by the fact that both AFM and TEM data indicate only small variations in the size of the nanoparticles, which is not enough to justify a 50-70 nm blue-shift of the SPR transition. High-resolution transmission electron microscopy (HRTEM) and selected area electron diffraction (SAED) studies further confirm the absence of Cu(II)-containing CuNPs when prepared in the presence of tetrazolate anions.

## Introduction

Excitation of the Surface Plasmon Resonance (SPR) electronic transition in metallic nanoparticles (MNPs) has shown to be particularly useful in guiding the synthesis and modification of a diverse range of nanostructures<sup>1-5</sup> and plasmonic metamaterials.<sup>6, 7</sup> Plasmonically-active metal nanoparticles have been used as catalysts,<sup>8-10</sup> chemical probes<sup>11, 12</sup> and to enhance the efficiency of solar cells.<sup>13-17</sup> Application of the fascinating optical and electronic properties of MNPs arising from excitation of surface plasmons has been enhanced by the controlled growth of novel MNP morphologies.<sup>18-21</sup> Tunable and broadband plasmonic absorption can be achieved by controlling the MNP dimensions.<sup>3, 22</sup> Tunability of the plasmon resonances in metal-oxide nanocrystals has been demonstrated by cooperative cation-anion codoping.<sup>23</sup>

However, challenges associated with reproducibly synthesizing complex nanostructures, including nanostars and nanoflowers, has restricted more widespread application of the plasmonic properties of these complex MNPs.<sup>24</sup> Encapsulation of less complex plasmonic nanostructures, predominantly nanospheres, with chelating ligands has seen the development of new catalytic pathways for chemical and biological transformations.<sup>25-28</sup> For instance, electronic interactions between the MNP surface and surrounding fluorophores has been shown to result in fluorescence enhancement,<sup>29-32</sup> quenching<sup>33</sup> and switching.<sup>34</sup>

Copper nanoparticles (CuNPs) are becoming increasingly attractive as plasmon catalysts due to both their physical and chemical properties, including plasmonic transitions in the visible spectral region, and because of the relatively low cost and abundant copper ore reserves on Earth.<sup>35</sup> However, much less is known about CuNPs than noble-metal based NPs. In this paper we report on studies that demonstrate how the oxidation state of Cu surface atoms can be controlled by forming CuNPs in the presence of a specific class of encapsulating N-donor ligands, tetrazoles, in

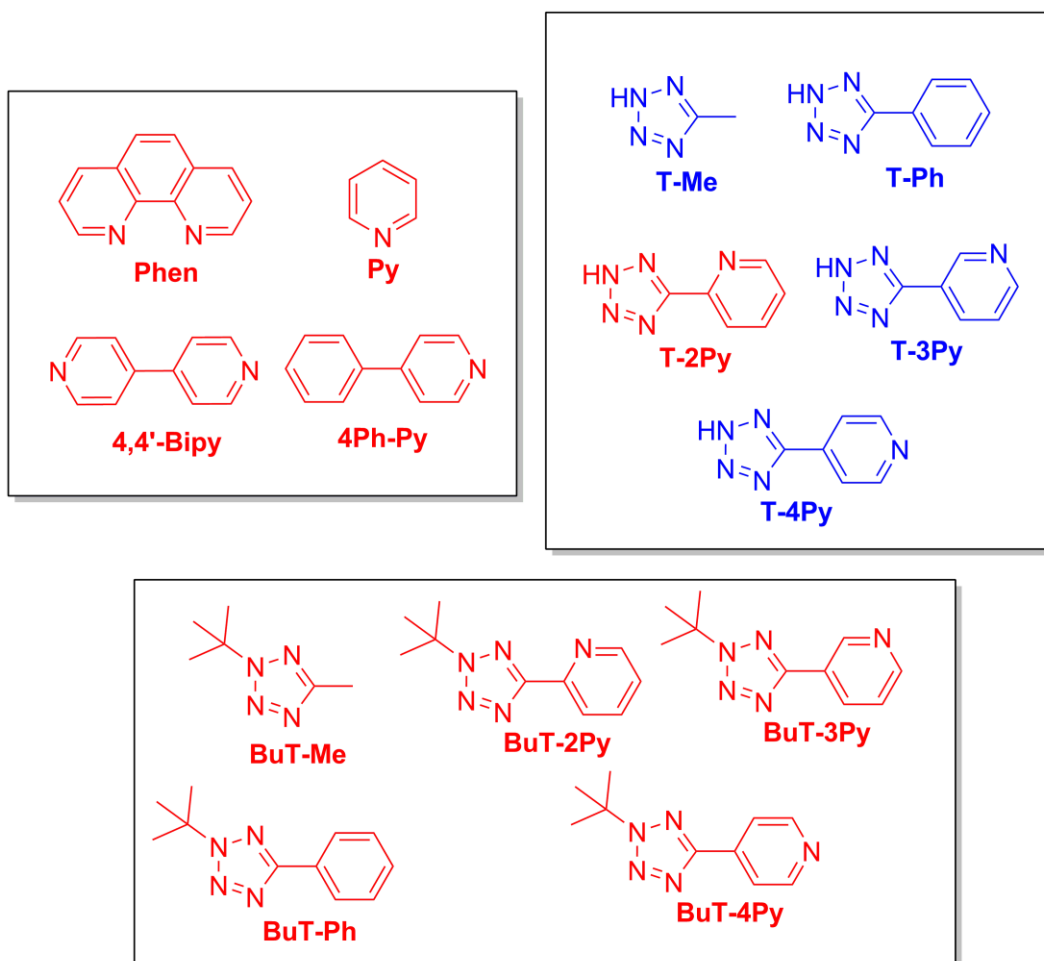
aqueous solution. Since the SPR transition is influenced by the surface chemical composition of the CuNPs, this strategy represents a facile methodology for the modulation of the SPR transition, which can be blue shifted up to 70 nm with respect to CuNPs formed in the absence of any encapsulating ligand.

CuNPs are produced by a technique we refer to as Laser Ablation Synthesis in Solution (LASiS).<sup>36, 37</sup> The technique involves focused laser irradiation of a bulk metal target in a liquid. The LASiS technique has grown in popularity in recent years, with the technique demonstrating nanoparticle production advantages including wide applicability to the production of a variety of nanomaterials in high yield with relative simplicity.<sup>38</sup> The ability to avoid the use of metal salt reduction agents also affords a significant “green” advantage to the LASiS technique.<sup>38, 39</sup>

Previous LASiS studies from our laboratory have involved the production of gold nanoparticles encapsulated by anionic<sup>36, 40</sup> and cationic<sup>37</sup> surfactants in aqueous solution; the present study involves the production of copper nanoparticles encapsulated by N-donor ligands in aqueous solution. The motivation for the study is to explore the fundamental chemistry involved in CuNP production in the presence of N-donor ligands via the LASiS approach. In particular, we are interested in how the N-donor ligands influence the formation of CuNPs via LASiS. These studies highlight an exciting new avenue for ligand-based tuning of the plasmonic properties of simple copper nanoparticles.

The structures and abbreviated names of the N-donor ligands used in this study are reported in Scheme 1. The ligands are grouped as pyridine-based, tetrazole-based, and alkylated tetrazole-based species. The major difference between these three classes of molecules is represented by the fact that tetrazoles can deprotonate in aqueous media, thus forming “electron-rich” anionic tetrazolates. In this regard, tetrazoles are often considered as isosteres of carboxylic acids ( $pK_a \approx$

5).<sup>41</sup> Each ligand in Scheme 1 is colored red or blue to indicate the relative shift of the CuNP SPR transition (see Results and Discussion).



**Scheme 1.** Formulations of the encapsulating ligands and their corresponding abbreviations used in this study. Ligands are colored red or blue to indicate the relative shift in wavelength of the CuNP SRP transition absorption maximum.

## Experimental Methods

### *N-donor ligands*

Phenanthroline (**Phen**), 4,4'-bipyridine (**4,4'Bipy**), pyridine (**Py**), 4-phenylpyridine (**4Ph-Py**) and 1H-5-methyltetrazole (**T-Me**) were obtained from Sigma Aldrich and used as received without any further purification. 1H-5-(4-pyridyl)tetrazole (**T-4Py**),<sup>42</sup> 2-tertbutyl-5-(4-pyridyl)tetrazole (**BuT-4Py**),<sup>42</sup> 1H-5-phenyltetrazole (**T-Ph**),<sup>43</sup> 1H-5-(3-pyridyl)tetrazole (**T-3Py**),<sup>43</sup> 1H-5-(2-pyridyl)tetrazole (**T-2Py**),<sup>44</sup> 2-tertbutyl-5-methyltetrazole (**BuT-Me**),<sup>45</sup> 2-tertbutyl-5-phenyltetrazole (**BuT-Ph**),<sup>45</sup> and 2-tertbutyl-5-(2-pyridyl)tetrazole (**BuT-2Py**),<sup>46</sup> were prepared according to previously published procedures. Following the procedure reported by Steel and co-workers,<sup>46</sup> 2-tertbutyl-5-(3-pyridyl)tetrazole (**BuT-3Py**) was obtained as a white solid; yield 94%. Nuclear magnetic resonance spectra, consisting of <sup>1</sup>H and <sup>13</sup>C, were recorded using a Bruker Avance 400 spectrometer (400.1 MHz for <sup>1</sup>H, 100 MHz for <sup>13</sup>C) at 300 K. <sup>1</sup>H and <sup>13</sup>C chemical shifts were referenced to residual solvent signals. <sup>1</sup>H-NMR (CDCl<sub>3</sub>) δ/ppm: 9.39 (1H, s), 8.71 (1H, d, J = 4.8 Hz), 8.48 (1H, d, J = 7.6 Hz), 7.46 (1H, dd, J = 7.8, 4.8 Hz), 1.81 (9H, s); <sup>13</sup>C-NMR (CDCl<sub>3</sub>) δ/ppm: 162.2 (CN<sub>4</sub>) 151.0, 148.2, 134.1, 124.2, 123.6, 64.3 (CMe<sub>3</sub>), 29.4 (CH<sub>3</sub>)

### *Copper Nanoparticle Formation*

The LASiS experimental method employed in our laboratory has been previously reported, including schematic representations of the experimental arrangement employed.<sup>36, 37, 40</sup> Only salient details are reported here. CuNPs were prepared in a manner similar to that reported by Haram and Ahmad,<sup>47</sup> either in ultrapure water (purified with a Lab PURE Plus UV system) or in the presence of a variety of N-donor ligands at a concentration of  $1 \times 10^{-4}$  M. Laser ablation is performed for 60 minutes at 1064 nm using a Continuum Surelite II Nd:YAG laser operating at 10 Hz and 7.5 mJ/pulse. The copper substrate is high purity, electronic grade oxygen-free copper



alloy C101 (99.99%). UV-visible absorption spectra of samples prepared by the method described above following 60 minutes of 1064 nm irradiation were recorded using a Cary 4000 UV-vis spectrometer.

#### *Atomic Force Microscopy (AFM) and Transmission Electron Microscopy (TEM)*

All samples synthesized following 60 min of 1064 nm irradiation were prepared for atomic force microscopic (AFM) analysis. The nanoparticles were deposited via spin coating for 4 minutes at 2000 rpm on a freshly cleaved mica substrate for the AFM analysis. AFM topography measurements were performed using a Dimension FastScan AFM system (Bruker, California, USA) in Tapping Mode operation. AFM probes of type TESPA (Bruker, California, USA) with a resonant frequency of 320 kHz, a spring constant of 42 N/m and a tip radius of 8 nm were used for the acquisition of all AFM data. The data were processed and analyzed with the Gwyddion AFM analysis software program.<sup>48</sup> Processing steps included data leveling by mean plane subtraction, horizontal scar correction and a plane level. If needed a 2<sup>nd</sup> degree polynomial background subtraction was executed. The size distribution data of the imaged nanoparticles was extracted from the height distribution, *i.e.*, the diameter, of the nanoparticles, the data then being processed in Sigmaplot<sup>™</sup> to generate the size distributions.

As a calibration of the particle size distributions determined via AFM, selected ligated CuNP samples were also characterized by transmission electron microscopy (see Supporting Information for particle size distributions). TEM experiments were undertaken on a Jeol 2011 electron microscope. A drop of CuNP solution was deposited on a Formvar-coated 100 mesh nickel grid and dried at room temperature. The TEM images were captured at an emission energy of 200 kV and magnification of 200,000X. Images were collected using a digital camera with supplier-

provided software, and all recorded images were analyzed using the ImageJ™ analysis program to determine particle sizes, and SigmaPlot™ to generate the size distributions.

#### *HRTEM, STEM and SAED*

High-Resolution TEM (HRTEM), Scanning TEM (STEM) and Selected Area Electron Diffraction (SAED) experiments were performed on an FEI Talos F200S GT TEM electron microscope. The Cu nanoparticle samples formed in the presence of ligands were diluted by a factor of 2 and sonicated, before a single drop of CuNP solution was deposited on a 300-mesh lacey carbon-coated grid and air dried. The HRTEM images were captured with an emission energy of 200 kV.

#### *X-ray Photoelectron Spectroscopy (XPS)*

Samples synthesized following 60 min of 1064 nm irradiation were also prepared for X-ray photoelectron spectroscopic (XPS) analysis. One drop of solution was placed upon a Pt-coated wafer. Solvent was removed from samples under reduced pressure and left to dry in a desiccator.

Samples were not purified, for example via centrifugation or dialysis, prior to XPS analysis. Optical spectroscopy control experiments, whereby the addition of tetrazole ligands to solutions of bare CuNPs produced via LASiS does not shift the position of the SPR transition, indicate that free ligands have no influence on CuNP surface chemistry post-LASiS.

The XPS experiments were performed on a Kratos Axis Ultra spectrometer equipped with an Al  $K_{\alpha}$  monochromatic X-ray source running at 15 kV, a hemispherical electron energy analyzer, and a multichannel detector. The test chamber pressure was maintained below  $2 \times 10^{-9}$  Torr during spectral acquisition.

The XPS binding energy (BE) was internally referenced to the aliphatic C (1s) peak (BE, 284.6 eV). Survey spectra were acquired at an analyzer pass energy of 100 eV, while high-resolution spectra were acquired with a pass energy of 20 eV.

Consistent with previous studies from our laboratory,<sup>49</sup> spectra were analyzed by fitting each peak with Gaussian-Lorentz functions after subtracting the background using the CasaXPS data processing software package<sup>50</sup> under the constraint of setting a reasonable BE shift and characteristic full width at half-maximum range. Atomic concentrations were calculated by normalizing peak areas to the elemental sensitivity factor data provided by the CasaXPS database.

## Results and Discussion

In a manner consistent with previous reports from our laboratory on the formation and stability of gold nanoparticles,<sup>36, 37, 40</sup> CuNPs are directly prepared in aqueous solution by laser ablation.<sup>47, 51</sup> Whilst the SPR peak position of all MNPs is affected by particle size and shape, the SPR peak position and intensity in CuNPs is reported to be particularly susceptible to oxidation at the NP surface, with the formation of Cu<sub>2</sub>O and CuO.<sup>52-54</sup>

The UV-vis absorption spectrum of CuNPs in pure water, produced after 60 minutes of 1064 nm laser irradiation (at 10 Hz, see Experimental Methods), is shown as the grey trace in Figure 1. The spectrum has been normalized for the maximum intensity of the SPR transition. The SPR transition has an absorption maximum at approximately 650 nm, reportedly indicative of oxidation of the nanoparticle surface.<sup>54</sup> Long and co-workers have demonstrated that the peak of the SPR transition shifts to approximately 580 nm upon removal of the CuNP oxide layer by treatment with glacial acetic acid.<sup>54</sup> All experiments reported herein have been undertaken under identical conditions, with the only variable being the nature of the N-donor ligand present in solution during the laser-

based production of CuNPs. We thus assume, at this initial stage, that all CuNP samples are similarly oxidized during their production.

Also presented in Figure 1 are the normalized UV-visible spectra of CuNP samples prepared in  $1 \times 10^{-4}$  M aqueous solutions of **Phen** (solid red line), **4,4'Bipy** (long-dashed line), **Py** (medium dashed line) and **4Ph-Py** (short-dashed line). Inspection of Figure 1 indicates that CuNPs prepared in the presence of the pyridine-based ligands display a SPR peak at wavelengths of approximately 630 nm, only slightly blue shifted from that of CuNPs prepared in pure water.<sup>†</sup> This suggests that the surface chemical composition and electron density is very similar for CuNPs formed in pure water or the presence of pyridine-based ligands.

SPR-normalized UV-visible spectra of CuNP samples prepared in  $1 \times 10^{-4}$  M aqueous solutions of the tetrazole-based ligands **T-Me**, **T-Ph**, **T-3Py** and **T-4Py** are presented in Figure 2, along with that of CuNPs produced in pure water (grey trace). It is clear that these ligands induce a significant blue shift of the encapsulated CuNP SPR peak of 50-70 nm (to approximately 580-600 nm).<sup>‡</sup> Based upon the report of Long and co-workers,<sup>54</sup> we attribute this spectral shift to oxidation state changes of the CuNP surface atoms. This preliminary attribution will be expanded upon later in this study. Nonetheless, this is a unique demonstration of the potentially profound influence of the encapsulating ligand on the plasmonic behavior of the laser-formed metal nanoparticle.

To test the hypothesis that the deprotonated form of the tetrazoles, formed in solution via acid-base equilibrium, induces the dramatic blue shifts in the CuNP SPR spectra, the corresponding

---

<sup>†</sup> We color these spectra red to indicate no significant SPR spectral shift compared to CuNPs produced in pure water.

<sup>‡</sup> We color these spectra blue to indicate a significant SPR spectral blue shift compared to CuNPs produced in pure water.

*tert*-butylated tetrazole ligands were used as encapsulating agents. SPR-normalized UV-visible spectra of CuNP samples prepared in  $1 \times 10^{-4}$  M aqueous solutions of **BuT-Me**, **BuT-Ph**, **BuT-3Py** and **BuT-4Py** are presented in Figure 3, along with that of CuNPs produced in pure water (grey trace). With these *tert*-butylated encapsulating ligands being unable to deprotonate, the encapsulated CuNP SPR peak absorption is not significantly blue shifted, in a similar fashion to the results presented in Figure 1 for the pyridine-based ligands. Indeed, the SPR maximum absorption wavelength of **BuT-Ph** (long-dashed line in Figure 3) is very slightly red shifted relative to that of ‘bare’ CuNPs produced in pure water.

Interestingly, the SPR-normalized UV-visible spectrum of CuNP samples prepared in  $1 \times 10^{-4}$  M aqueous solutions of **T-2Py** also displays only a moderate blue shift from the SPR of bare CuNP (Figure 4; solid red line), even though this species belongs to the tetrazole-based group. We rationalize this outlier behavior by considering the predominant form of the pyridyl-tetrazole molecules in an aqueous environment. Prior to deprotonation, the regioisomers **T-3Py** and **T-4Py** are likely to exist in their charge-separated zwitterionic forms, bearing a negatively charged tetrazolate ring along with a positively charged pyridium substituent. While this can also occur on **T-2Py**, the protonation and deprotonation sites are spatially adjacent, thus effectively forming a “chelated” proton. This limits the charge separation and avoids the formal formation of a tetrazolate anion as experienced by **T-3Py** and **T-4Py**. Evidence to support this assertion is provided by the UV-visible absorption spectrum of **BuT-2Py**, which is also presented in Figure 4 (dashed line). Clearly, the zwitterionic form of **T-2Py** does not significantly increase the electron density on the tetrazole as much as the other ligands of this group.

Optical scattering contributions may influence the position of SPR transitions in nanomaterials. These scattering effects can have a stronger influence at higher energies (shorter wavelengths)

relative to the SPR transitions.<sup>55, 56</sup> We observe no compelling evidence to suggest that scattering effects influence the position of SPR transitions in this study. SPR-normalized optical spectra for a selection CuNP samples presented in Figures 2, 3 and 4 are reproduced over the wavelength range 400 – 850 nm and presented in Supporting Information Figure S1 (**T-2Py**, **BuT-2Py**, **BuT-3Py**, and **But-4Py**) and Figure S2 (**T-Me**, **T-Ph**, **T-3Py**, and **T-4Py**). All spectra in Figures S1 and S2 display similar wavelength dependencies at higher transition energies.

The peak position of the SPR transition in MNPs is also influenced by nanoparticle size.<sup>57</sup> However, El-Sayed and co-workers have reported consistently that for gold nanoparticles of diameters less than approximately 20 nm, this effect is not expected to be significant.<sup>58-60</sup> Rice *et al.* discuss how copper and gold can be expected to behave in a similar manner due to both metals having similar band structures and optical properties.<sup>61</sup> Moreover, these workers demonstrate that changes in CuNP optical properties can be primarily attributed to changes in surface oxidation rather than NP size. Sun *et al.* demonstrate that CuNPs synthesized with diameters of 7.5 nm and 12.2 nm display very similar absorption spectra.<sup>62</sup> Finally, El-Sayed and co-workers show that CuNPs with diameters of 12 nm and 30 nm display nearly identical absorption spectra.<sup>63</sup> Therefore, we do not expect the spectral blue shifts evident in Figure 2 to be attributable to significantly smaller particle size distributions for CuNPs produced via LASiS in the presence of the tetrazole-based ligand solutions. Nonetheless, determination of CuNP particle size distributions is required as confirmation.

To confirm that the 50-70 nm SPR spectral blue shifts are not the result of different CuNP particle size distributions being produced in the presence of tetrazole-based encapsulating ligands, particle size distributions have been measured via both AFM and TEM. Representative particle size distributions and associated cumulative distribution functions from AFM measurements for

bare CuNPs and for those formed in the presence of selected ligands are presented in Figure 5. AFM-determined particle size distributions for all other ligands used in this study are presented in the Supporting Information (Figures S3-S6). To improve the statistics of the particle-size distribution determinations, each histogram was generated by analyzing multiple images (see Experimental Method for details). All samples have been analyzed via AFM measurements. Selected ligand-encapsulation samples, together with CuNPs prepared in pure water, were also analyzed via TEM to ensure confidence in particle size determinations via an independent method. All TEM data are presented in the Supporting Information (Figures S7-S8). The samples analyzed via TEM include CuNPs prepared in pure water as well as in ligand solutions that result in no significant SPR spectral shift and those that do. Comparison of the data presented in Figure 5 together with that in the Supporting Information indicates that the AFM and TEM results are in good agreement.

The particle size distributions for bare CuNPs and those encapsulated with **Py** are very similar (see Figure 5), with the former having a maximum in the size distribution of 8 nm. The latter exhibits a size distribution maximum of 6 nm and is a little narrower, as indicated by the sharper cumulative distribution function. The two distributions of CuNPs encapsulated with **T-3Py** and **BuT-3Py** exhibit slightly smaller and narrower distributions, with maxima of 3 nm and 5 nm for **T-3Py** and **BuT-3Py**, respectively. Together, the relative consistency of CuNP size distributions generated in this study and the previously reported observations of El-Sayed and co-workers<sup>63</sup> indicate that the observed SPR spectral shifts displayed in Figure 2 cannot be attributed to differences in CuNP particle size.

Having eliminated significant differences in the encapsulated CuNP particle size distributions as the cause of the 50-70 nm blue shift in the CuNP SPR transition maximum for the tetrazole-

based ligands, it is prudent to consider whether the ability of these ligands to deprotonate in aqueous solution may be the primary factor influencing the CuNP surface electron density, and thus the SPR absorption maximum. To test this possibility, CuNPs were generated via the LASiS approach in solutions of  $1 \times 10^{-4}$  M benzoic and nicotinic acid. Both ligands have similar  $pK_a$  values to the tetrazoles reported in Figure 2 and might therefore be expected to bring about similar spectral shifts to the blue if this phenomenon is attributable to ligand deprotonation in aqueous solution.

The UV-visible spectra of CuNPs generated in benzoic and nicotinic acid solutions are presented in Figure 6. The CuNP SPR transition for the case of benzoic acid encapsulation is extremely similar to those for CuNP formed in the presence of pyridine-based and alkylated-tetrazole based ligands. In the case of the pyridine-based and alkylated-tetrazole based ligands a very slight blue shift to bare CuNPs in water is observed, whereas for the nicotinic acid encapsulation a very slight red shift to bare CuNPs is observed. The conclusion that must be drawn is that the 50-70 nm blue shift in the SPR transition for CuNPs formed in the presence of tetrazole-based ligands arises from the presence of the anionic tetrazolate species rather than the presence of a weak acid characterized by a  $pK_a \approx 5$ . It is likely that the presence of the anionic tetrazolate moiety influences nascent CuNP formation during the LASiS process. We assert this *in situ* effect because control experiments whereby the addition of these tetrazole ligands to solutions of bare CuNPs produced via LASiS does not influence the position of the SPR transition. The spectral shifts are only observed when the CuNPs are formed in the presence of these ligands.

Reports in the literature<sup>52-54, 61</sup> indicate that the “red” CuNP SPR transition around 650 nm can be attributed to the presence of an oxide layer at the CuNP surface, while the “blue” CuNP SPR transition around 580 nm is attributable to an oxide-free CuNP surface. Based upon this possibility,



we have used the classical Tauc approach<sup>64, 65</sup> to estimate the optical energy band gaps of the oxide-layer containing encapsulated CuNPs. Specifically, we have taken the approach reported by Ng and Fan,<sup>66</sup> which is based on the earlier reports characterizing semiconductor band gaps by Chang *et al.*<sup>67</sup> and Fukuda and co-workers.<sup>68</sup>

In brief, we use the following equation for semiconductors:

$$\alpha(\nu) = A \left( \frac{h\nu}{2} - E_g \right)^{m/2}$$

where  $\alpha$  is the optical absorption coefficient at excitation frequency  $\nu$ ,  $A$  is a constant and  $m = 1$  for an allowed direct transition.<sup>67</sup> Figure 7 shows a series of plots of  $(\alpha \text{eV})^2$  versus photon energy ( $E_{\text{photon}}$ , eV) under these conditions. In each case the extrapolated value (the straight lines to the  $x$ -axis) of  $E_{\text{photon}}$  at  $\alpha = 0$  gives an absorption edge energy corresponding to the optical band gap energy,  $E_g$ . The representative plots in Figure 7 correspond to the same encapsulation conditions as for the particle size distributions presented in Figure 5. The band gap values determined for all encapsulation conditions are reported in Table 1. The equivalent plots to those presented in Figure 7 for all encapsulation conditions are provided in the Supporting Information (Figures S9-S11).

Inspection of the band gap values reported in Table 1 clearly highlights that the four tetrazole ligands, *viz.*, **T-Me**, **T-Ph**, **T-3Py** and **T-4Py**, have a larger band gap than all other ligands or indeed for bare CuNPs in aqueous solution. All of the band gap values reported in Table 1 are larger than that for single-crystal Cu<sub>2</sub>O (2.1722 eV),<sup>69</sup> which is consistent with the nanoparticles not forming well-defined crystal structures, especially in terms of thin surface oxide surface layers. However, the larger band gap values for the CuNPs formed in the presence of tetrazole ligands is suggestive of relatively lower levels of surface oxide formation. Such an outcome would be consistent with the literature reports of these CuNPs exhibiting blue-shifted SPR transitions because of oxide-free surfaces.<sup>52-54, 61</sup>

To characterize the surface chemistry of CuNPs formed in the presence of all ligands, XPS measurements were undertaken, with particular attention placed on exploring the copper, oxygen, and nitrogen signals (see Experimental Methods for details). Not surprisingly, for all samples analyzed, except for the bare CuNPs, a strong nitrogen (1s) signal is observed. All samples also display a strong oxygen (1s) signal. Such a result is inconsistent with the aforementioned claims of the blue-shifted SPR arising from oxide-free CuNPs. Thus, careful analysis of the copper (2p<sub>3/2</sub>) signal for all samples was undertaken.

For each recorded XPS spectrum, the data were deconvoluted to obtain the relative population of each copper oxidation state. This was achieved by fitting the spectra to a sum of peaks using non-linear least squares minimization. A Shirley background was applied to remove the electron scattering background and maintain the intrinsic line shape from the raw data.<sup>70</sup> A pseudo-Voigt function comprised of the sum of Gaussian (30%) and Lorentzian (70%) functions was used, following the approach described by Biesinger *et al.*<sup>71</sup> In this approach, as the binding energies (BE) of Cu(0) and Cu(I) are unresolvable, these two oxidation states are considered to generate a single emission peak. Thus, a determination is made between the relative proportion of Cu(II) versus the sum of Cu(0) plus Cu(I) (which we now refer to as ‘Cu(0+I)’) contributing to both the main 2p<sub>3/2</sub> transition and its associated satellite (or ‘shake-up’) transition according to:

$$\%Cu(II) = \frac{B + A1}{A + B} \times 100$$

where A1 represents the contribution of Cu(II) to the main 2p<sub>3/2</sub> transition and A represents the sum of Cu(II) and Cu(0+I). By contrast only Cu(II) contributes to the shake-up transition, represented as B in the equation above. The total intensity from Cu(II) species is represented in the combination of the signals from the direct photoelectron emission (A1) and the shake-up photoelectron emission (B), as schematically shown in Figure 8.

X-ray photoelectron spectra for the representative **BuT-3Py** and **T-3Py** encapsulation ligands are presented in Figure 9, panels a and b, respectively. Each spectrum displays the Cu  $2p_{3/2}$  transition region, together with the fitted components as described above. It is apparent in Figure 9a that both Cu(0+I) and Cu(II) transitions are present in the direct photoelectron emission transition at lower binding energies (between approximately 931-937 eV; the Cu(II) contribution is evident as the high-energy shoulder). Moreover, the higher energy shake-up peak, arising from the presence of Cu(II) at the CuNP surface, is clearly evident (approx. 940-947 eV). The appearance of this high-energy Cu  $2p_{3/2}$  satellite transition is also evident for the bare CuNPs produced in aqueous solution as well as for all ligand encapsulation conditions except for the four tetrazole-based ligands (see Supporting Information; Figures S12-S13). The equivalent XPS spectrum for cases of CuNPs formed in the presence of tetrazoles is represented in Figure 9b (for **T-3Py**). Here, there is no evidence of a Cu(II) shoulder in the main transition and no evidence at all of the Cu(II) shake-up transition. The equivalent fitted XPS spectra for the cases of all the tetrazole-based ligands, where no Cu(II) signal is observed, are also reported in the Supporting Information (Figures S13-S14).

In Table 2 we present the %Cu(II) determined from the above analysis, together with the SPR transition  $\lambda_{\text{max}}$ , for each ligation scenario explored in this study. We have already confirmed that the blue shift in the SPR  $\lambda_{\text{max}}$  is not attributable to the presence or absence of an oxide layer on the CuNP surface due to the observation of a significant O ( $1s$ ) signal in all XPS spectra. Rather, the blue shift is clearly correlated with the absence of Cu(II) in CuNPs formed via LASiS. That is, the production of nascent CuNPs in the presence of the deprotonated tetrazole ligands suppresses the formation of Cu(II) at the nanoparticle surface. As a reminder, the absence of Cu(II) occurs during

the nanoparticle formation process because adding these ligands to bare CuNP samples post-LASiS does not bring about the spectral shift to the blue.

The presence of an oxide layer on all CuNP surfaces determined in this study is consistent with the results of several laser-based CuNP production studies.<sup>47, 72, 73</sup> Haram and Ahmad discuss the formation of copper hydroxide following the laser-induced Cu plasma plume reacting with solvent water, with subsequent decomposition to copper oxides.<sup>47</sup> Gondal *et al.* report similar outcomes, with Cu(I) being ultimately partially oxidized to Cu(II).<sup>72</sup> Each of these studies build upon the initial report by Tilaki *et al.* where Cu(II) oxides were shown to be formed via laser ablation in water, but not when using acetone as the solvent.<sup>73</sup>

The aforementioned studies support the putative suggestion that the deprotonated tetrazoles in aqueous solution act as a reducing agent, preventing the formation of Cu(II) during LASiS production. Such behavior by these ligands would be akin to the reducing behavior of compounds such as hydrazine during traditional chemical reduction CuNP formation.<sup>74, 75</sup> Hydrazine is known to differentially coordinate to Cu (111), (100) and (110) surfaces,<sup>76</sup> and potentially influence CuNP size and shape during nanoparticle formation.<sup>77</sup>

To test the assertion that tetrazolate anions act as *in situ* reducing agents during the LASiS production of CuNPs, LASiS experiments were undertaken in the presence of  $1 \times 10^{-4}$  M aqueous hydrazine solution. The resultant SPR-normalized UV-visible absorption spectrum is presented in Figure 10. This clearly shows an equivalent blue spectral shift evident for CuNPs formed in the presence of deprotonated tetrazole ligands. Moreover, the associated XPS analysis also shows that 0% Cu(II) is found on the CuNP surfaces (see Table 2).

To further explore the oxidation chemistry of the CuNPs, SAED and HRTEM studies were undertaken on a small selection of the samples in this study. Cu nanoparticles adopt a face centered

cubic (fcc) structure, and upon oxidation they may partially or completely convert into copper oxides such as Cu<sub>2</sub>O and CuO alongside a re-arrangement of the crystal structure.<sup>78</sup> Such structural changes can be verified through the analyses of the SAED patterns and HRTEM images of the corresponding samples. Specifically, SAED pattern analysis allows the lattice planes of Cu, Cu<sub>2</sub>O, and CuO to be indexed, and the surface oxidation states of CuNPs can therefore be determined. Furthermore, the lattice plane spacings visualized in HRTEM images can be indexed to Cu or copper oxide species such as Cu<sub>2</sub>O and CuO.

Figure 11 compares TEM images and the associated SAED patterns of CuNP samples prepared in (a) pure water, (b) **4,4'Bipy**, (c) **T-4Py**, and (d) **BuT-4Py**. All images show that spherical nanoparticles are formed, with particle sizes in the range of 5 to 30 nm. A close inspection on these products reveals that the use of the **4,4'Bipy** (Figure 11b), **T-4Py** (Figure 11c), and **BuT-4Py** (Figure 11d) capping ligands does not influence the CuNP size and morphology compared with those produced in pure water (Figure 1a). A STEM image of CuNPs prepared in the presence of **T-4Py** shows that the nanoparticles have a spherical shape, which is consistent with the results of the TEM images in Figure 11c (see Supporting Information; Figure S15).

The coexistence of Cu, Cu<sub>2</sub>O and CuO in the samples presented in Figure 11 is further confirmed by the presence of distinct diffraction patterns in the SAED of the particles. The corresponding interplanar spacings for each diffraction pattern are 0.289, 0.240, 0.203, 0.169, 0.146 and 0.124 nm, which correspond to CuO (110), Cu<sub>2</sub>O (111), Cu (111), Cu (200), Cu<sub>2</sub>O (220) and Cu (220), respectively (Table 3). The interplanar spacing of 0.203 nm has been assigned to both Cu<sub>2</sub>O (200) and Cu (111) because these lattice plane spacings are very close and hard to differentiate in the SAED patterns. It is worth noting that the diffraction pattern with an interplanar spacing of 0.289 nm corresponding, CuO (110), is not apparent in the CuNPs prepared in the solution using **T-4Py**

as the capping ligand (Figure 11c). This provides clear and strong evidence that no CuO-containing CuNPs are produced when **T-4Py** is used as the capping ligand. This result is consistent with the observation of the blue shift in the SPR due to the absence of Cu(II) in nanoparticles formed via LASiS.

Figures 12 and 13 show HRTEM images of nanoparticles prepared via LASiS using **T-4Py** as the capping ligand. Nanoparticles obtained have either a slightly elongated shape (1 in Figure 12a) or spherical shape (2 in Figure 12a). Lattice fringes with spacings of 0.299, 0.24 and 0.21 nm are clearly seen and are indexed into CuO (110), Cu<sub>2</sub>O (111), and Cu (111)/ Cu<sub>2</sub>O (200), respectively (Figures 12b and 12c). The lattice spacing of 0.17 nm of the nanoparticle in Figure 13 is assigned to the (200) lattice plane of Cu (0). The HRTEM results further confirm the absence of Cu(II) nanoparticles in the sample prepared in the solution using **T-4Py** as the capping ligand.

Importantly, the HR-TEM data presented in Figure 12 show no evidence for the formation of graphitic matrix effects. Such effects are commonly observed under LASiS conditions involving organic solvents, such as toluene.<sup>79, 80</sup> They are not observed in LASiS experiments performed in water. The nitrogen-rich ligand concentration of  $1 \times 10^{-4}$  M in aqueous solution employed in these studies is highly unlikely to produce a graphitic matrix. Moreover, a simple control experiment from our laboratory involving LASiS irradiation of ligand solutions in the absence of a metal disk for 1 hour shows no decomposition of the ligands, as measured by <sup>1</sup>H NMR spectroscopy.<sup>81</sup> This indicates that the high intensity photon regime does not cause photodegradation of the tetrazole ligands, which would be required to generate graphitic layers.

Together, the above data provide compelling evidence in support of the presence of deprotonated tetrazolate moieties providing a reducing environment during the LASiS-based production of CuNPs that prevents the formation of Cu(II) on the NP surface. The mechanism for formation of

nanomaterials during laser ablation in liquids has been extensively studied, both experimentally<sup>82, 83</sup> and theoretically.<sup>84, 85</sup> The temperature inside the ablation plume where CuNPs are formed is suggested to be as high as 5700 K.<sup>84</sup> The formation of the nanostructures is attributed to the combination of ultrafast quenching of a hot plasma within the ablation plume and its interaction with the surrounding medium.<sup>86</sup> High temperatures at the plasma plume front result in excitation and evaporation of the surrounding liquid. This incorporates both solvent and solute molecules into the outer edge of the plasma, often referred to as a plasma-induced pressure region.<sup>83</sup> Our investigations suggest that this interfacial region is where the reduction of Cu(II) occurs within nascent CuNPs.

Our results offer a novel pathway for controlling the surface oxidation of laser-formed CuNPs and is a particularly striking outcome because tetrazolate anions are routinely considered to be relatively stable ligands in terms of their redox behavior in the presence of redox-active metal cations. For example, it is well documented that the addition of tetrazolate anions to Cu(II) precursors leads to the formation of stable Cu(II) complexes rather than to a reduction of the metal center.<sup>87</sup>

## Conclusions

We have demonstrated, for the first time, how the surface plasmon resonance (SPR) in laser-formed copper nanoparticles (CuNPs) is systematically controlled by the electronic structure of encapsulating N-donor ligands present in solution. We have demonstrated that anionic tetrazolates formally act as a reducing agent during the laser-based formation of the CuNPs. Formation of the CuNPs under these reducing conditions prevents the formation of Cu(II) at the nanoparticle surface, which is manifest as a significant (50-70 nm) spectral blue shift in the CuNP SPR

transition maximum and is confirmed by HRTEM and SAED studies. This *in situ* reduction is achieved without changes to CuNP size or shape. These studies highlight a useful avenue, using readily accessible species such as tetrazoles, for controlling the optical properties of simple NP architectures, obviating the need to synthesize complex nanoarchitectures.

## Supporting Information

Figures S1 – S15. Expanded wavelength UV-visible spectra, additional AFM-determined CuNP particle size distributions, additional TEM-determined CuNP particle size distributions, additional plots of  $(\alpha E_{\text{photon}})^2$  versus  $E_{\text{photon}}$  for CuNPs formed in the presence of various ligand solutions, additional fitted XPS spectra for the Cu ( $2p_{3/2}$ ) transition for CuNPs formed in the presence of various ligand solutions, and STEM image of CuNPs prepared in the presence of **T-4Py**.

## Acknowledgement

The authors gratefully acknowledge the financial support of the Australian Research Council and Curtin University, as well as Professor Andrew Lowe for helpful discussions. The authors also acknowledge the use of equipment, scientific and technical assistance of the WA X-Ray Surface Analysis Facility, funded by the Australian Research Council LIEF grant LE120100026.

## References

(1) Langille, M. R.; Personick, M. L.; Mirkin, C. A. Plasmon-Mediated Syntheses of Metallic Nanostructures. *Angew. Chem. Int. Ed.* **2013**, 52 (52), 13910-13940, DOI: 10.1002/anie.201301875.



(2) Mangelson, B. F.; Jones, M. R.; Park, D. J.; Shade, C. M.; Schatz, G. C.; Mirkin, C. A. Synthesis and Characterization of a Plasmonic–Semiconductor Composite Containing Rationally Designed, Optically Tunable Gold Nanorod Dimers and Anatase TiO<sub>2</sub>. *Chem. Mat.* **2014**, *26* (12), 3818-3824, DOI: 10.1021/cm5014625.

(3) Mangelson, B. F.; Park, D. J.; Ku, J. C.; Osberg, K. D.; Schatz, G. C.; Mirkin, C. A. Tunable and Broadband Plasmonic Absorption via Dispersible Nanoantennas with Sub-10 nm Gaps. *Small* **2013**, *9* (13), 2250-2254, DOI: 10.1002/smll.201202787.

(4) Zheng, J. P.; Cheng, X. Z.; Zhang, H.; Bai, X. P.; Ai, R. Q.; Shao, L.; Wang, J. F. Gold Nanorods: The Most Versatile Plasmonic Nanoparticles. *Chem. Rev.* **2021**, *121* (21), 13342-13453, DOI: 10.1021/acs.chemrev.1c00422.

(5) Agrawal, A.; Cho, S. H.; Zandi, O.; Ghosh, S.; Johns, R. W.; Milliron, D. J. Localized Surface Plasmon Resonance in Semiconductor Nanocrystals. *Chem. Rev.* **2018**, *118* (6), 3121-3207, DOI: 10.1021/acs.chemrev.7b00613.

(6) Young, K. L.; Ross, M. B.; Blaber, M. G.; Rycenga, M.; Jones, M. R.; Zhang, C.; Senesi, A. J.; Lee, B.; Schatz, G. C.; Mirkin, C. A. Using DNA to Design Plasmonic Metamaterials with Tunable Optical Properties. *Adv. Mater.* **2014**, *26* (4), 653-659, DOI: 10.1002/adma.201302938.

(7) Gilroy, K. D.; Ruditskiy, A.; Peng, H. C.; Qin, D.; Xia, Y. N. Bimetallic Nanocrystals: Syntheses, Properties, and Applications. *Chem. Rev.* **2016**, *116* (18), 10414-10472, DOI: 10.1021/acs.chemrev.6b00211.

- (8) Sellappan, R.; Nielsen, M. G.; González-Posada, F.; Vesborg, P. C. K.; Chorkendorff, I.; Chakarov, D. Effects of Plasmon Excitation on Photocatalytic Activity of Ag/TiO<sub>2</sub> and Au/TiO<sub>2</sub> Nanocomposites. *J. Catal.* **2013**, *307*, 214-221, DOI: 10.1016/j.jcat.2013.07.024.
- (9) Gelle, A.; Jin, T.; de la Garza, L.; Price, G. D.; Besteiro, L. V.; Moores, A. Applications of Plasmon-Enhanced Nanocatalysis to Organic Transformations. *Chem. Rev.* **2020**, *120* (2), 986-1041, DOI: 10.1021/acs.chemrev.9b00187.
- (10) Yamashita, H.; Mori, K.; Kuwahara, Y.; Kamegawa, T.; Wen, M. C.; Verma, P.; Che, M. Single-Site and Nano-Confined Photocatalysts Designed in Porous Materials for Environmental Uses and Solar Fuels. *Chem. Soc. Rev.* **2018**, *47* (22), 8072-8096, DOI: 10.1039/c8cs00341f.
- (11) Jain, P. K.; Manthiram, K.; Engel, J. H.; White, S. L.; Fauchaux, J. A.; Alivisatos, A. P. Doped Nanocrystals as Plasmonic Probes of Redox Chemistry. *Angew. Chem. Int. Ed.* **2013**, *52* (51), 13671-13675, DOI: 10.1002/anie.201303707.
- (12) Shaik, F.; Peer, I.; Jain, P. K.; Amirav, L. Plasmon-Enhanced Multicarrier Photocatalysis. *Nano Lett.* **2018**, *18* (7), 4370-4376, DOI: 10.1021/acs.nanolett.8b01392.
- (13) Noh, H. S.; Cho, E. H.; Kim, H. M.; Han, Y. D.; Joo, J. Organic Solar Cells Using Plasmonics of Ag Nanoprisms. *Org. Electron.* **2013**, *14* (1), 278-285, DOI: 10.1016/j.orgel.2012.10.040.
- (14) Sebo, B.; Huang, N.; Liu, Y.; Tai, Q.; Liang, L.; Hu, H.; Xu, S.; Zhao, X.-Z. Dye-Sensitized Solar Cells Enhanced by Optical Absorption, Mediated by TiO<sub>2</sub> Nanofibers and Plasmonics Ag Nanoparticles. *Electrochim. Acta* **2013**, *112*, 458-464, DOI: 10.1016/j.electacta.2013.08.167.

- (15) Tong, C.; Yun, J.; Song, H.; Gan, Q.; Anderson, W. A. Plasmonic-Enhanced Si Schottky Barrier Solar Cells. *Sol. Energy Mater. Sol. Cells* **2014**, *120*, 591-595, DOI: 10.1016/j.solmat.2013.10.001.
- (16) Rai, P. Plasmonic Noble Metal@Metal Oxide Core-Shell Nanoparticles for Dye-Sensitized Solar Cell Applications. *Sustain. Energ. Fuels* **2019**, *3* (1), 63-91, DOI: 10.1039/c8se00336j.
- (17) Pradhan, N.; Das Adhikari, S.; Nag, A.; Sarma, D. D. Luminescence, Plasmonic, and Magnetic Properties of Doped Semiconductor Nanocrystals. *Angew. Chem. Int. Ed.* **2017**, *56* (25), 7038-7054, DOI: 10.1002/anie.201611526.
- (18) Liao, H. G.; Jiang, Y. X.; Zhou, Z. Y.; Chen, S. P.; Sun, S. G. Shape-Controlled Synthesis of Gold Nanoparticles in Deep Eutectic Solvents for Studies of Structure-Functionality Relationships in Electrocatalysis. *Angew. Chem. Int. Ed.* **2008**, *47* (47), 9100-9103, DOI: 10.1002/anie.200803202.
- (19) Golze, S. D.; Hughes, R. A.; Rouvimov, S.; Neal, R. D.; Demille, T. B.; Neretina, S. Plasmon-Mediated Synthesis of Periodic Arrays of Gold Nanoplates Using Substrate-Immobilized Seeds Lined with Planar Defects. *Nano Lett.* **2019**, *19* (8), 5653-5660, DOI: 10.1021/acs.nanolett.9b02215.
- (20) Mukherji, S.; Bharti, S.; Shukla, G.; Mukherji, S. Synthesis and Characterization of Size- and Shape-Controlled Silver Nanoparticles. *Phys. Sci. Rev.* **2019**, *4* (1), 73, DOI: 10.1515/psr-2017-0082.

- (21) Kamarudheen, R.; Castellanos, G. W.; Kamp, L. P. J.; Clercx, H. J. H.; Baldi, A. Quantifying Photothermal and Hot Charge Carrier Effects in Plasmon-Driven Nanoparticle Syntheses. *ACS Nano* **2018**, *12* (8), 8447-8455, DOI: 10.1021/acsnano.8b03929.
- (22) Zhou, W.; Gao, H.; Odom, T. W. Toward Broadband Plasmonics: Tuning Dispersion in Rhombic Plasmonic Crystals. *ACS Nano* **2010**, *4* (2), 1241-1247, DOI: 10.1021/nn901590p.
- (23) Ye, X.; Fei, J.; Diroll, B. T.; Paik, T.; Murray, C. B. Expanding the Spectral Tunability of Plasmonic Resonances in Doped Metal-Oxide Nanocrystals through Cooperative Cation-Anion Codoping. *J. Am. Chem. Soc.* **2014**, *136* (33), 11680-11686, DOI: 10.1021/ja5039903.
- (24) Shen, J.; Xu, L.; Wang, C.; Pei, H.; Tai, R.; Song, S.; Huang, Q.; Fan, C.; Chen, G. Dynamic and Quantitative Control of the DNA-Mediated Growth of Gold Plasmonic Nanostructures. *Angew. Chem. Int. Ed.* **2014**, *53* (32), 8338-8342, DOI: 10.1002/anie.201402937.
- (25) Cai, X.; Anyaogu, K. C.; Neckers, D. C. Photopolymerization of Conductive Polymeric Metal Nanoparticles. *Photochem. Photobiol. Sci.* **2009**, *8* (11), 1568-1573, DOI: 10.1039/b9pp00043g.
- (26) Kaur, R.; Giordano, C.; Gradzielski, M.; Mehta, S. K. Synthesis of Highly Stable, Water-Dispersible Copper Nanoparticles as Catalysts for Nitrobenzene Reduction. *Chem. Asian J.* **2014**, *9* (1), 189-198, DOI: 10.1002/asia.201300809.
- (27) Wang, Z.; von dem Bussche, A.; Kabadi, P. K.; Kane, A. B.; Hurt, R. H. Biological and Environmental Transformations of Copper-Based Nanomaterials. *ACS Nano* **2013**, *7* (10), 8715-8727, DOI: 10.1021/nn403080y.

- (28) Xie, J. J.; Ping, H.; Tan, T. N.; Lei, L. W.; Xie, H.; Yang, X. Y.; Fu, Z. Y. Bioprocess-Inspired Fabrication of Materials with New Structures and Functions. *Prog. Mater. Sci.* **2019**, *105*, 49, DOI: 10.1016/j.pmatsci.2019.05.004.
- (29) Basheer, N. S.; Kumar, B. R.; Kurian, A.; George, S. D. Silver Nanoparticle Size-Dependent Measurement of Quantum Efficiency of Rhodamine 6G. *Appl. Phys. B* **2013**, *113* (4), 581-587, DOI: 10.1007/s00340-013-5513-3.
- (30) Chung, H. Y.; Leung, P. T.; Tsai, D. P. Molecular Fluorescence in the Vicinity of a Charged Metallic Nanoparticle. *Opt. Express* **2013**, *21* (22), 26483-26492, DOI: 10.1364/OE.21.026483.
- (31) Li, C.; Zhu, J. Metal-Enhanced Fluorescence of OG-488 Doped in Au@SiO<sub>2</sub> Core-Shell Nanoparticles. *Mater. Lett.* **2013**, *112*, 169-172, DOI: 10.1016/j.matlet.2013.09.021.
- (32) Li, J.; Zhu, J.-J.; Xu, K. Fluorescent Metal Nanoclusters: From Synthesis to Applications. *TrAC-Trends Anal. Chem.* **2014**, *58*, 90-98, DOI: 10.1016/j.trac.2014.02.011.
- (33) Chowdhury, S.; Bhethanabotla, V. R.; Sen, R. Quenching of Fluorescence from CdSe/ZnS Nanocrystal QDs Near Copper Nanoparticles in Aqueous Solution. *Plasmonics* **2011**, *6* (4), 735-740, DOI: 10.1007/s11468-011-9257-9.
- (34) Garcia-Amoros, J.; Swaminathan, S.; Sortino, S.; Raymo, F. M. Plasmonic Activation of a Fluorescent Carbazole-Oxazine Switch. *Chem. Eur. J.* **2014**, *20* (33), 10276-10284, DOI: 10.1002/chem.201403509.
- (35) Xin, Y.; Yu, K. F.; Zhang, L. T.; Yang, Y. R.; Yuan, H. B.; Li, H. L.; Wang, L. B.; Zeng, J. Copper-Based Plasmonic Catalysis: Recent Advances and Future Perspectives. *Adv. Mater.* **2021**, *33* (32), 26, DOI: 10.1002/adma.202008145.

(36) Fong, Y.-Y.; Gascooke, J. R.; Visser, B. R.; Metha, G. F.; Buntine, M. A. Laser-Based Formation and Properties of Gold Nanoparticles in Aqueous Solution: Formation Kinetics and Surfactant-Modified Particle Size Distributions. *J. Phys. Chem. C* **2010**, *114* (38), 15931-15940, DOI: 10.1021/jp9118315.

(37) Fong, Y. Y.; Gascooke, J. R.; Visser, B. R.; Harris, H. H.; Cowie, B. C.; Thomsen, L.; Metha, G. F.; Buntine, M. A. Influence of Cationic Surfactants on the Formation and Surface Oxidation States of Gold Nanoparticles Produced via Laser Ablation. *Langmuir* **2013**, *29* (40), 12452-12462, DOI: 10.1021/la402234k.

(38) Coviello, V.; Forrer, D.; Amendola, V. Recent Developments in Plasmonic Alloy Nanoparticles: Synthesis, Modelling, Properties and Applications. *ChemPhysChem* **2022**, *23* (21), 40, DOI: 10.1002/cphc.202200136.

(39) Rafique, M.; Rafique, M. S.; Kalsoom, U.; Afzal, A.; Butt, S. H.; Usman, A. Laser Ablation Synthesis of Silver Nanoparticles in Water and Dependence on Laser Nature. *Opt. Quantum Electron.* **2019**, *51* (6), 11, DOI: 10.1007/s11082-019-1902-0.

(40) Fong, Y.-Y.; Gascooke, J. R.; Metha, G. F.; Buntine, M. A. Influence of Surfactant Concentration on Laser-Based Gold Nanoparticle Formation and Stability. *Aust. J. Chem.* **2012**, *65* (2), 97-104, DOI: 10.1071/ch11366.

(41) Werrett, M. V.; Chartrand, D.; Gale, J. D.; Hanan, G. S.; MacLellan, J. G.; Massi, M.; Muzzioli, S.; Raiteri, P.; Skelton, B. W.; Silberstein, M.; et al. Synthesis, Structural, and Photophysical Investigation of Diimine Triscarbonyl Re(I) Tetrazolato Complexes. *Inorg. Chem.* **2011**, *50* (4), 1229-1241, DOI: 10.1021/ic1015516.

(42) Wright, P. J.; Muzzioli, S.; Werrett, M. V.; Raiteri, P.; Skelton, B. W.; Silvester, D. S.; Stagni, S.; Massi, M. Synthesis, Photophysical and Electrochemical Investigation of Dinuclear Tetrazolato-Bridged Rhenium Complexes. *Organometallics* **2012**, *31* (21), 7566-7578, DOI: 10.1021/om300870a.

(43) Koguro, K.; Oga, T.; Mitsui, S.; Orita, R. Novel Synthesis of 5-Substituted Tetrazoles from Nitriles. *Synthesis* **1998**, 910-914, DOI: 10.1055/s-1998-2081.

(44) Fiorini, V.; Ranieri, A. M.; Muzzioli, S.; Magee, K. D.; Zacchini, S.; Akabar, N.; Stefan, A.; Ogden, M. I.; Massi, M.; Stagni, S. Targeting Divalent Metal Cations with Re(I) Tetrazolato Complexes. *Dalton Trans.* **2015**, *44* (47), 20597-20608, DOI: 10.1039/c5dt03690a.

(45) Lisakova, A. D.; Ryabukhin, D. S.; Trifonov, R. E.; Ostrovskii, V. A.; Vasilyev, A. V. Alkylation of 5-Substituted NH-Tetrazoles by Alcohols in the Superacid CF<sub>3</sub>SO<sub>3</sub>H. *Tetrahedron Lett.* **2015**, *56* (50), 7020-7023, DOI: 10.1016/j.tetlet.2015.11.005.

(46) Downard, A. J.; Steel, P. J.; Steenwijk, J. Syntheses of Chelating Tetrazole-Containing Ligands and Studies of their Palladium (II) and Ruthenium (II) Complexes. *Aust. J. Chem.* **1995**, *48* (9), 1625-1642.

(47) Haram, N.; Ahmad, N. Effect of Laser Fluence on the Size of Copper Oxide Nanoparticles Produced by the Ablation of Cu Target in Double Distilled Water. *Appl. Phys. A* **2012**, *111* (4), 1131-1137, DOI: 10.1007/s00339-012-7329-0.

(48) Nečas, D.; Klapetek, P. Gwyddion: An Open-Source Software for SPM Data Analysis. *Open Phys.* **2012**, *10* (1), 181-188, DOI: 10.2478/s11534-011-0096-2.

(49) Fong, Y. Y.; Visser, B. R.; Gascooke, J. R.; Cowie, B. C.; Thomsen, L.; Metha, G. F.; Buntine, M. A.; Harris, H. H. Photoreduction Kinetics of Sodium Tetrachloroaurate under Synchrotron Soft X-ray Exposure. *Langmuir* **2011**, 27 (13), 8099-8104, DOI: 10.1021/la200463k.

(50) Fairley, N.; Carrick, A. *The CASA Cookbook Recipes for XPS Data Processing, Pt. 1*; Acolyte Science, 2005.

(51) Kumar, B.; Thareja, R. K. Laser Ablated Copper Plasmas in Liquid and Gas Ambient. *Phys. Plasmas* **2013**, 20 (5), 6, DOI: 10.1063/1.4807041.

(52) Chan, G. H.; Zhao, J.; Hicks, E. M.; Schatz, G. C.; Van Duyne, R. P. Plasmonic Properties of Copper Nanoparticles Fabricated by Nanosphere Lithography. *Nano Lett.* **2007**, 7 (7), 1947-1952, DOI: 10.1021/nl070648a.

(53) Gonzalez-Posada, F.; Sellappan, R.; Vanpoucke, B.; Chakarov, D. Oxidation of Copper Nanoparticles in Water Monitored *in situ* by Localized Surface Plasmon Resonance Spectroscopy. *RSC Adv.* **2014**, 4 (40), 20659-20664, DOI: 10.1039/c3ra47473a.

(54) Qin, L. X.; Jing, C.; Li, Y.; Li, D. W.; Long, Y. T. Real-Time Monitoring of the Aging of Single Plasmonic Copper Nanoparticles. *Chem. Commun.* **2012**, 48 (10), 1511-1513, DOI: 10.1039/c1cc14326c.

(55) Coskun, M.; Altinoz, S.; Coskun, O. D. Optical Properties of VO<sub>2</sub> Spherical Nanoparticles. *Photonics Nanostruct.* **2022**, 49, 9, DOI: 10.1016/j.photonics.2022.100993.

(56) Qian, X. H.; Park, H. S. The Influence of Mechanical Strain on the Optical Properties of Spherical Gold Nanoparticles. *J. Mech. Phys. Solids* **2010**, 58 (3), 330-345, DOI: 10.1016/j.jmps.2009.12.001.



(57) Bohren, C. F.; Huffman, D. R. *Absorption and Scattering of Light by Small Particles*; Wiley-Interscience, 1983.

(58) Link, S.; El-Sayed, M. A. Spectral Properties and Relaxation Dynamics of Surface Plasmon Electronic Oscillations in Gold and Silver Nanodots and Nanorods. *J. Phys. Chem. B* **1999**, *103* (40), 8410-8426, DOI: 10.1021/jp9917648.

(59) Link, S.; El-Sayed, M. A. Shape and Size Dependence of Radiative, Non-Radiative and Photothermal Properties of Gold Nanocrystals. *Int. Rev. Phys. Chem.* **2000**, *19* (3), 409-453, DOI: 10.1080/01442350050034180.

(60) Link, S.; El-Sayed, M. A. Optical Properties and Ultrafast Dynamics of Metallic Nanocrystals. *Annu. Rev. Phys. Chem.* **2003**, *54*, 331-366, DOI: 10.1146/annurev.physchem.54.011002.103759.

(61) Rice, K. P.; Walker, E. J.; Stoykovich, M. P.; Saunders, A. E. Solvent-Dependent Surface Plasmon Response and Oxidation of Copper Nanocrystals. *J. Phys. Chem. C* **2011**, *115* (5), 1793-1799, DOI: 10.1021/jp110483z.

(62) Sun, Q. C.; Ding, Y.; Goodman, S. M.; Funke, H. H.; Nagpal, P. Copper Plasmonics and Catalysis: Role of Electron-Phonon Interactions in Dephasing Localized Surface Plasmons. *Nanoscale* **2014**, *6* (21), 12450-12457, DOI: 10.1039/c4nr04719b.

(63) Darugar, Q.; Qian, W.; El-Sayed, M. A.; Pileni, M. P. Size-Dependent Ultrafast Electronic Energy Relaxation and Enhanced Fluorescence of Copper Nanoparticles. *J. Phys. Chem. B* **2006**, *110* (1), 143-149, DOI: 10.1021/jp0545445.

(64) Tauc, J. Optical Properties and Electronic Structure of Amorphous Ge and Si. *Mat. Res. Bull.* **1968**, *3*, 37-46.

(65) Tauc, J.; Grigorovici, R.; Vancu, A. Optical Properties and Electronic Structure of Amorphous Germanium. *Phys. Stat. Sol.* **1966**, *15*, 627-637.

(66) Ng, C. H.; Fan, W. Y. Shape Evolution of Cu<sub>2</sub>O Nanostructures via Kinetic and Thermodynamic Controlled Growth. *J. Phys. Chem. B* **2006**, *110* (42), 20801-20807, DOI: 10.1021/jp061835k.

(67) Chang, Y.; Teo, J. J.; Zeng, H. C. Formation of Colloidal CuO Nanocrystallites and their Spherical Aggregation and Reductive Transformation to Hollow Cu<sub>2</sub>O Nanospheres. *Langmuir* **2005**, *21* (3), 1074-1079, DOI: 10.1021/la047671l.

(68) Tsunekawa, S.; Fukuda, T.; Kasuya, A. Blue Shift in Ultraviolet Absorption Spectra of Monodisperse CeO<sub>2-x</sub> nanoparticles. *J. Appl. Phys.* **2000**, *87* (3), 1318-1321, DOI: 10.1063/1.372016.

(69) Matsumoto, H.; Saito, K.; Hasuo, M.; Kono, S.; Nagasawa, N. Revived Interest on Yellow-Exciton Series in Cu<sub>2</sub>C: An Experimental Aspect. *Solid State Commun.* **1996**, *97* (2), 125-129, DOI: 10.1016/0038-1098(95)00601-x.

(70) Végh, J. The Shirley Background Revised. *J. Electron Spectrosc. Relat. Phenom.* **2006**, *151* (3), 159-164, DOI: 10.1016/j.elspec.2005.12.002.

(71) Biesinger, M. C.; Payne, B. P.; Grosvenor, A. P.; Lau, L. W. M.; Gerson, A. R.; Smart, R. S. C. Resolving Surface Chemical States in XPS Analysis of First Row Transition Metals, Oxides

and Hydroxides: Cr, Mn, Fe, Co and Ni. *Appl. Surf. Sci.* **2011**, 257 (7), 2717-2730, DOI: 10.1016/j.apsusc.2010.10.051.

(72) Gondal, M. A.; Qahtan, T. F.; Dastageer, M. A.; Saleh, T. A.; Maganda, Y. W.; Anjum, D. H. Effects of Oxidizing Medium on the Composition, Morphology and Optical Properties of Copper Oxide Nanoparticles Produced by Pulsed Laser Ablation. *Appl. Surf. Sci.* **2013**, 286, 149-155, DOI: 10.1016/j.apsusc.2013.09.038.

(73) Tilaki, R. M.; Iraji zad, A.; Mahdavi, S. M. Size, Composition and Optical Properties of Copper Nanoparticles Prepared by Laser Ablation in Liquids. *Appl. Phys. A* **2007**, 88 (2), 415-419, DOI: 10.1007/s00339-007-4000-2.

(74) Khodashenas, B.; Ghorbani, H. R. Synthesis of Copper Nanoparticles : An Overview of the Various Methods. *Korean J. Chem. Eng.* **2014**, 31 (7), 1105-1109, DOI: 10.1007/s11814-014-0127-y.

(75) Umer, A.; Naveed, S.; Ramzan, N.; Rafique, M. S. Selection of a Suitable Method for the Synthesis of Copper Nanoparticles. *Nano* **2012**, 07 (05), 18, DOI: 10.1142/s1793292012300058.

(76) Daff, T. D.; Costa, D.; Lisiecki, I.; de Leeuw, N. H. Density Functional Theory Calculations of the Interaction of Hydrazine with Low-Index Copper Surfaces. *J. Phys. Chem. C* **2009**, 113 (35), 15714-15722, DOI: 10.1021/jp904054n.

(77) Engels, V.; Benaskar, F.; Jefferson, D. A.; Johnson, B. F.; Wheatley, A. E. Nanoparticulate Copper--Routes Towards Oxidative Stability. *Dalton Trans.* **2010**, 39 (28), 6496-6502, DOI: 10.1039/c0dt00134a.

(78) Cheng, G. J.; Walker, A. R. H. Transmission Electron Microscopy Characterization of Colloidal Copper Nanoparticles and their Chemical Activity. *Anal. Bioanal. Chem.* **2010**, *396* (3), 1057-1069, DOI: 10.1007/s00216-009-3203-0.

(79) Amendola, V.; Polizzi, S.; Meneghetti, M. Laser Ablation Synthesis of Silver Nanoparticles Embedded in Graphitic Carbon Matrix. *Sci. Adv. Mater.* **2012**, *4* (3-4), 497-500, DOI: 10.1166/sam.2012.1308.

(80) Amendola, V.; Rizzi, G. A.; Polizzi, S.; Meneghetti, M. Synthesis of Gold Nanoparticles by Laser Ablation in Toluene: Quenching and Recovery of the Surface Plasmon Absorption. *J. Phys. Chem. B* **2005**, *109* (49), 23125-23128, DOI: 10.1021/jp055783v.

(81) Tilbury, R. D. Investigation into Electronic Interactions Between Tetrazolato Complexes and Metal Nanoparticles Synthesised via Laser Ablation. PhD Thesis, Curtin University, Perth, WA, 2017. <http://hdl.handle.net/20.500.11937/57109>.

(82) Niu, K. Y.; Yang, J.; Kulinich, S. A.; Sun, J.; Li, H.; Du, X. W. Morphology Control of Nanostructures via Surface Reaction of Metal Nanodroplets. *J. Am. Chem. Soc.* **2010**, *132* (28), 9814-9819, DOI: 10.1021/ja102967a.

(83) Yang, G. W. Laser Ablation in Liquids: Applications in the Synthesis of Nanocrystals. *Prog. Mater. Sci.* **2007**, *52* (4), 648-698, DOI: 10.1016/j.pmatsci.2006.10.016.

(84) Mazzi, A.; Gorrini, F.; Miotello, A. Dynamics of Liquid Nanodroplet Formation in Nanosecond Laser Ablation of Metals. *Appl. Surf. Sci.* **2017**, *418*, 601-606, DOI: 10.1016/j.apsusc.2016.09.006.

(85) Nyabadza, A.; Vazquez, M.; Brabazon, D. Modelling of Pulsed Laser Ablation in Liquid via Monte Carlo Techniques: The Effect of Laser Parameters and Liquid Medium on the Electron Cloud. *Solid State Sci.* **2022**, *133*, 11, DOI: 10.1016/j.solidstatesciences.2022.107003.

(86) Liu, P. S.; Cai, W. P.; Zeng, H. B. Fabrication and Size-Dependent Optical Properties of FeO Nanoparticles Induced by Laser Ablation in a Liquid Medium. *J. Phys. Chem. C* **2008**, *112* (9), 3261-3266, DOI: 10.1021/jp709714a.

(87) Saha, M.; Das, M.; Nasani, R.; Choudhuri, I.; Yousufuddin, M.; Nayek, H. P.; Shaikh, M. M.; Pathak, B.; Mukhopadhyay, S. Targeted Water Soluble Copper-Tetrazolate Complexes: Interactions with Biomolecules and Catecholase Like Activities. *Dalton Trans.* **2015**, *44* (46), 20154-20167, DOI: 10.1039/c5dt01471a.

**Table 1.** Optical band gaps determined via the classical Tauc approach for CuNPs produced under the specified ligand encapsulation conditions. See text for details.

<b>Encapsulating Ligand</b>	<b>Bandgap (eV)</b>
Bare CuNP	3.0
<b>Phen</b>	3.2
<b>4,4' Bipy</b>	3.1
<b>Py</b>	3.1
<b>4Ph-Py</b>	3.2
<b>T-Me</b>	3.6
<b>T-Ph</b>	3.9
<b>T-3Py</b>	3.9
<b>T-4Py</b>	3.7
<b>BuT-Me</b>	3.1
<b>BuT-Ph</b>	3.1
<b>BuT-3Py</b>	3.1
<b>BuT-4Py</b>	3.1
<b>T-2Py</b>	3.1
<b>BuT-2Py</b>	3.1
Benzoic Acid	3.1
Nicotinic Acid	2.9

**Table 2.** LASiS-formed CuNP SPR transition  $\lambda_{\text{max}}$  values, together with %Cu(II) determinations for each ligand encapsulation condition. See text for details.

Encapsulating Ligand	SPR $\lambda_{\text{max}}$ (nm)	%Cu(II)
Bare CuNP	655	28
<b>Phen</b>	630	23
<b>4,4' Bipy</b>	630	39
<b>Py</b>	635	32
<b>4Ph-Py</b>	640	55
<b>T-Me</b>	595	0
<b>T-Ph</b>	582	0
<b>T-3Py</b>	595	0
<b>T-4Py</b>	595	0
<b>BuT-Me</b>	650	18
<b>BuT-Ph</b>	675	32
<b>BuT-3Py</b>	640	48
<b>BuT-4Py</b>	640	28
<b>T-2Py</b>	630	58
<b>BuT-2Py</b>	640	32
Benzoic Acid	635	53
Nicotinic Acid	665	86
Hydrazine	590	0

**Table 3.** Lattice spacing and the corresponding Miller index extracted from the SEAD patterns of nanoparticles in Figure 11.

Bare CuNP		<b>4,4' Bipy</b>		<b>T-4Py</b>		<b>BuT-4Py</b>	
d spacing (nm)	Lattice plane (hkl)	d spacing (nm)	Lattice plane (hkl)	d spacing (nm)	Lattice plane (hkl)	d spacing (nm)	Lattice plane (hkl)
0.289	CuO(110)	0.285	CuO(110)			0.285	CuO(110)
0.240	Cu <sub>2</sub> O(111)	0.247	Cu <sub>2</sub> O(111)	0.240	Cu <sub>2</sub> O(111)	0.247	Cu <sub>2</sub> O(111)
0.203	Cu <sub>2</sub> O(200)	0.217	Cu <sub>2</sub> O(200)	0.203	Cu <sub>2</sub> O(200)	0.217	Cu <sub>2</sub> O(200)
	Cu(111)		Cu(111)		Cu(111)		Cu(111)
0.169	Cu(200)	0.178	Cu(200)	0.169	Cu(200)	0.178	Cu(200)
0.146	Cu <sub>2</sub> O(220)	0.145	Cu <sub>2</sub> O(220)	0.146	Cu <sub>2</sub> O(220)	0.145	Cu <sub>2</sub> O(220)
0.124	Cu(220)	0.123	Cu(220)	0.124	Cu(220)	0.123	Cu(220)



## Figure Captions

**Figure 1.** UV-visible absorption spectrum of CuNPs prepared in pure water by laser ablation for 60 minutes (grey trace). The SPR absorption peak at approx. 650 nm indicates oxidation of the CuNP surface. The solid red trace is the equivalent SPR-normalized absorption spectrum of CuNPs produced by laser ablation in a  $1 \times 10^{-4}$  M aqueous solution of **Phen**. The long-dashed line represents the SPR-normalized spectrum of CuNPs produced with **4,4' Bipy**; the medium-dashed line represents that for CuNPs produced with **Py**; the short-dashed line represents that for **4Ph-Py**.

**Figure 2.** SPR-normalized UV-visible absorption spectra of CuNPs prepared by laser ablation for 60 minutes in pure water (grey trace) and  $1 \times 10^{-4}$  M aqueous solutions of **T-Me** (upper solid line), **T-Ph** (long-dashed line), **T-3py** (medium-dashed line) and **T-4py** (short-dashed line).

**Figure 3.** SPR-normalized UV-visible absorption spectra of CuNPs prepared by laser ablation for 60 minutes in pure water (grey trace) and  $1 \times 10^{-4}$  M aqueous solutions of **BuT-Me** (solid red line), **BuT-Ph** (long-dashed line), **BuT-3Py** (medium-dashed line) and **BuT-4Py** (short-dashed line).

**Figure 4.** SPR-normalized UV-visible absorption spectra of CuNPs prepared by laser ablation for 60 minutes in pure water (grey trace) and  $1 \times 10^{-4}$  M aqueous solutions of **T-2Py** (solid red line) and **BuT-2Py** (dashed red line).

**Figure 5.** Particle size distributions and cumulative function distributions of bare CuNPs produced by the LASiS method, together with those from CuNPs encapsulated with **Py**, **T-3Py** and **BuT-3Py**. In the case of the bare CuNPs the size distribution has a maximum at 8 nm. The size distribution maximum for **Py**-encapsulated CuNPs is 6 nm, while that for T-3Py-encapsulated CuNPs is 3 nm and that for **BuT-3Py**-encapsulated CuNPs is 5 nm. Other size distribution statistics, including average particle sizes are include in the Supporting Information. See text for a discussion of these size distributions.

**Figure 6.** SPR-normalized UV-visible absorption spectra of CuNPs prepared by laser ablation for 60 minutes in pure water (grey trace) and  $1 \times 10^{-4}$  M aqueous solutions of benzoic acid (solid red line) and nicotinic acid (dashed red line).

**Figure 7.** Representative plots of  $(\alpha E_{\text{photon}})^2$  (where  $E_{\text{photon}}$  is reported in eV) versus  $E_{\text{photon}}$  for CuNPs formed in pure water (upper left), **Py** (upper right), **T-3Py** (lower left) and **BuT-3Py** (lower right). Optical band gap energies are determined by extrapolation of the linear region of each plot to  $\alpha = 0$  (y-axis intercept).

**Figure 8.** Schematic representation of the deconvolution components of the Cu ( $2p_{3/2}$ ) X-ray photoelectron spectra reported herein.

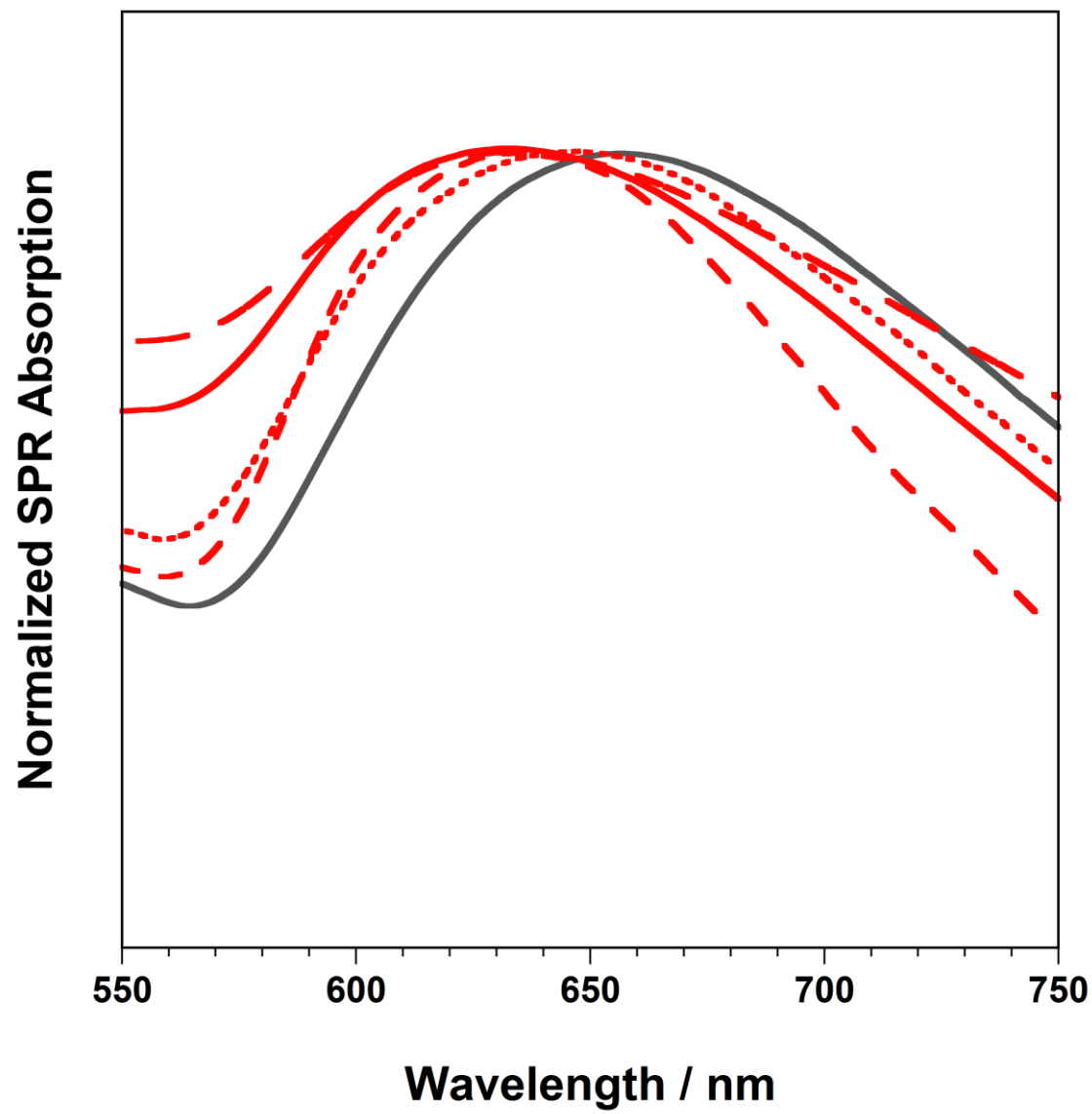
**Figure 9.** Fitted XPS spectra for the Cu ( $2p_{3/2}$ ) transition for CuNPs produced via LASiS in the presence of **BuT-3Py** (panel a) and **T-3Py** (panel b). See text for a discussion of the fitting procedure.

**Figure 10.** SPR-normalized UV-visible absorption spectra of CuNPs prepared by laser ablation for 60 minutes in pure water (grey trace) and  $1 \times 10^{-4}$  M aqueous solution of hydrazine (solid blue line).

**Figure 11.** TEM image and selected-area electron diffraction pattern of nanoparticles in (a) pure water, and in solutions of (b) **4,4' Bipy**, (c) **T-4Py** and (d) **BuT-4Py** as capping ligands.

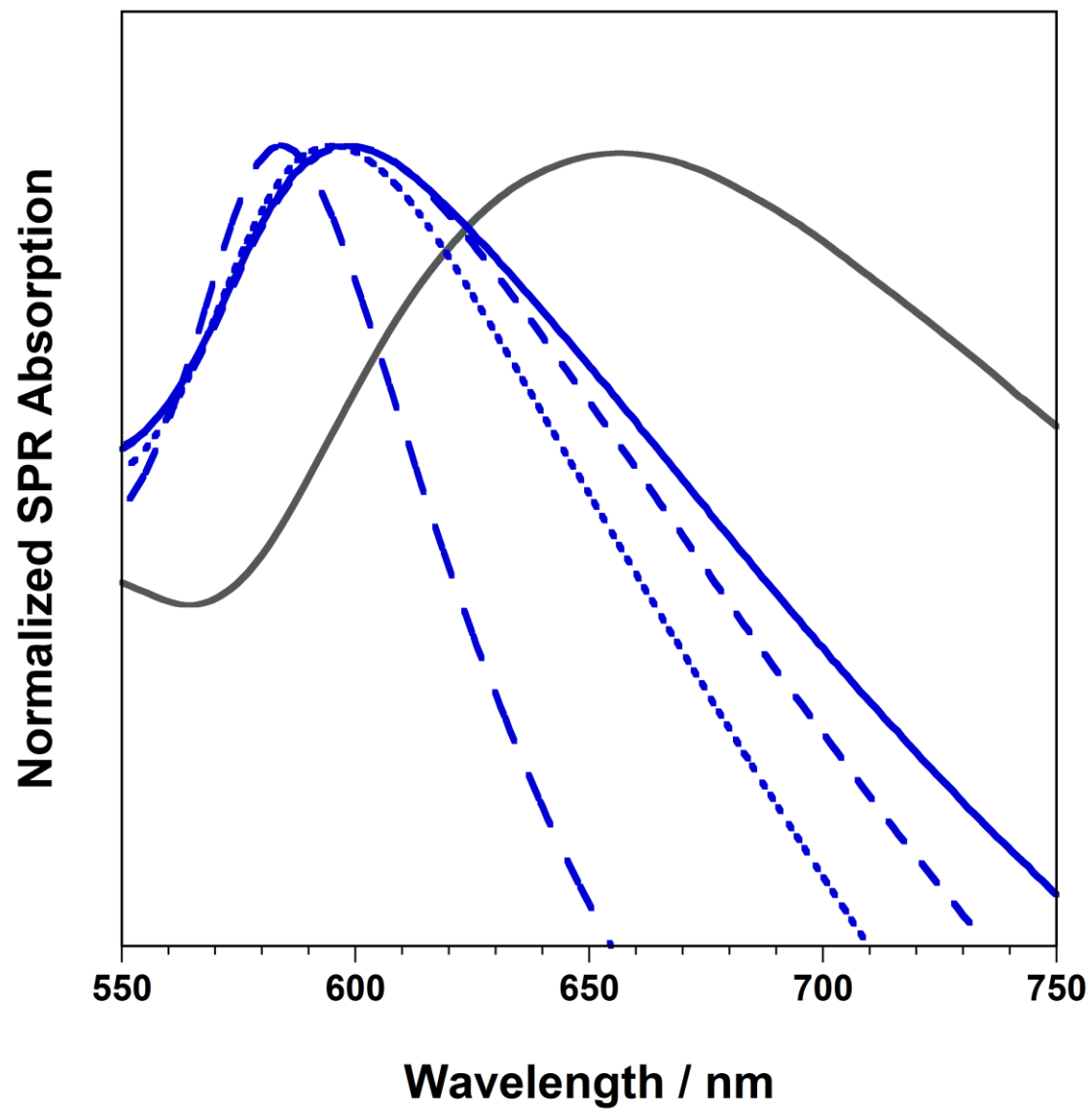
**Figure 12.** TEM and HRTEM images of Cu<sub>2</sub>O nanoparticles prepared in the presence of **T-4Py** as the capping ligand. (a) TEM image, (b) HRTEM image corresponding to the dashed rectangle 1 in (a), (c) HRTEM image corresponding to the dashed rectangle 2 in (a). White lines indicate the orientation of selected crystal planes.

**Figure 13.** HRTEM images of Cu nanoparticles prepared in the presence of **T-4Py** as the capping ligand. White lines indicate the orientation of selected crystal planes.



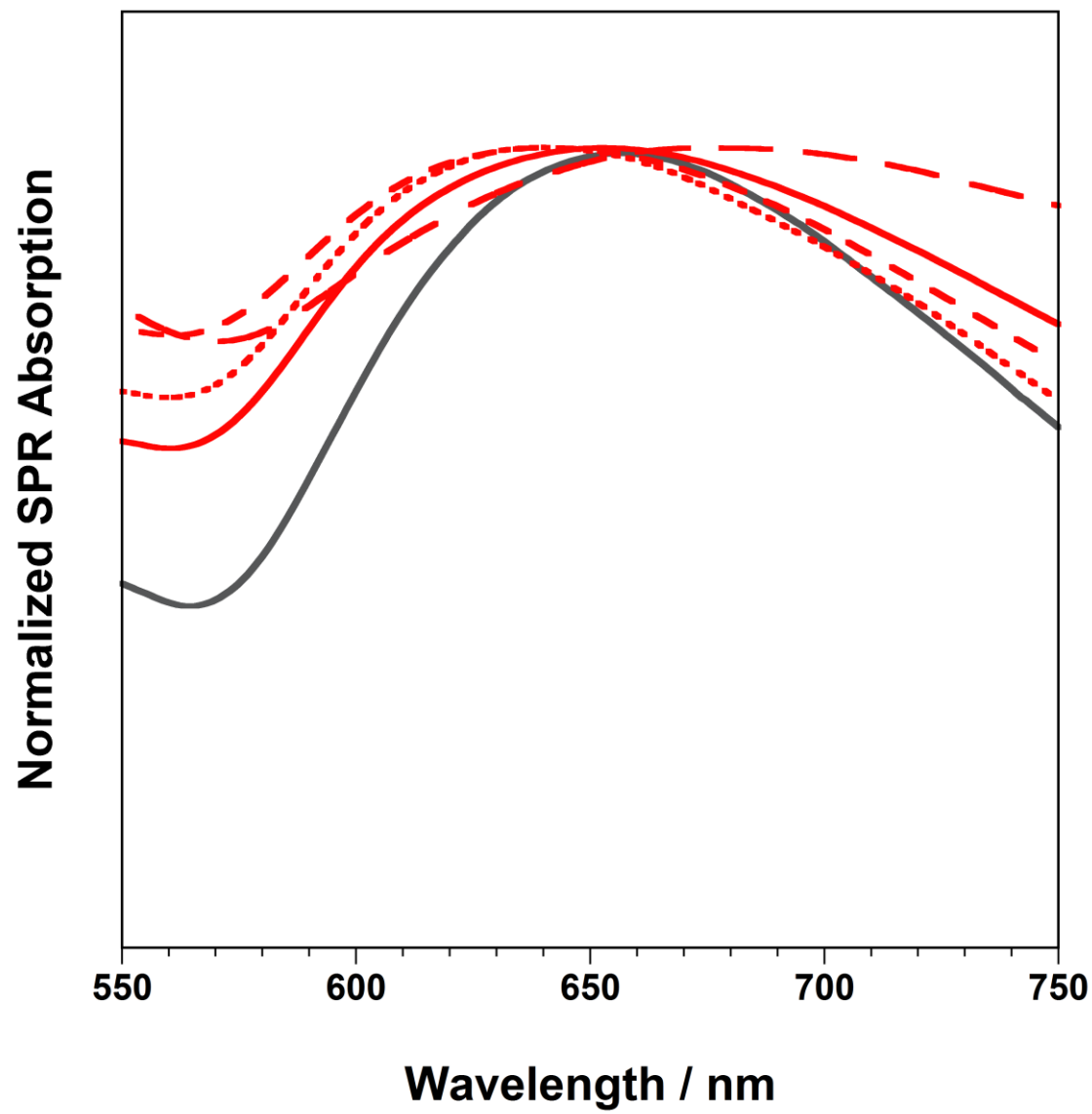
Mulder et al.

Figure 1



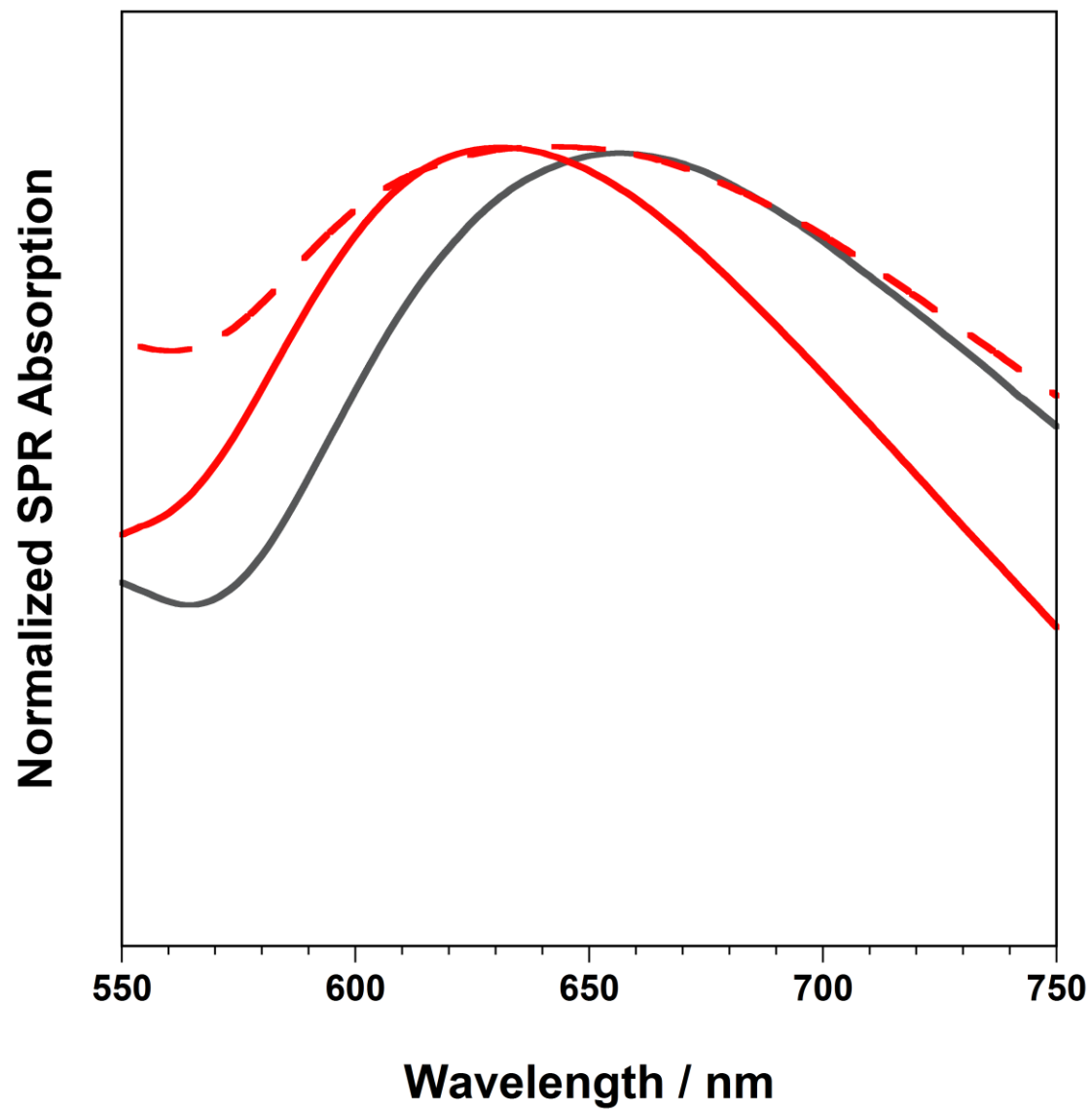
Mulder et al.

Figure 2



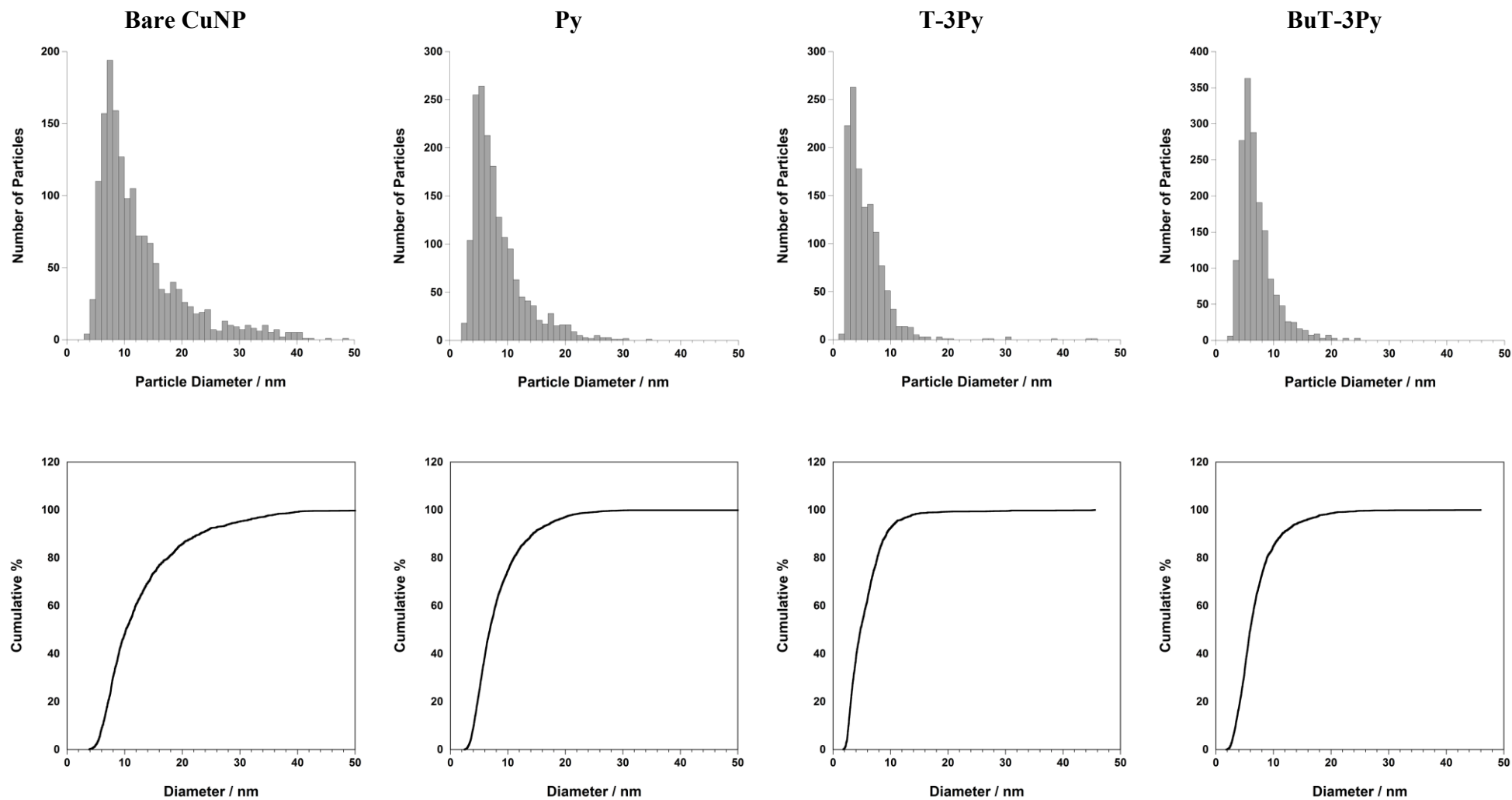
Mulder et al.

Figure 3



Mulder et al.

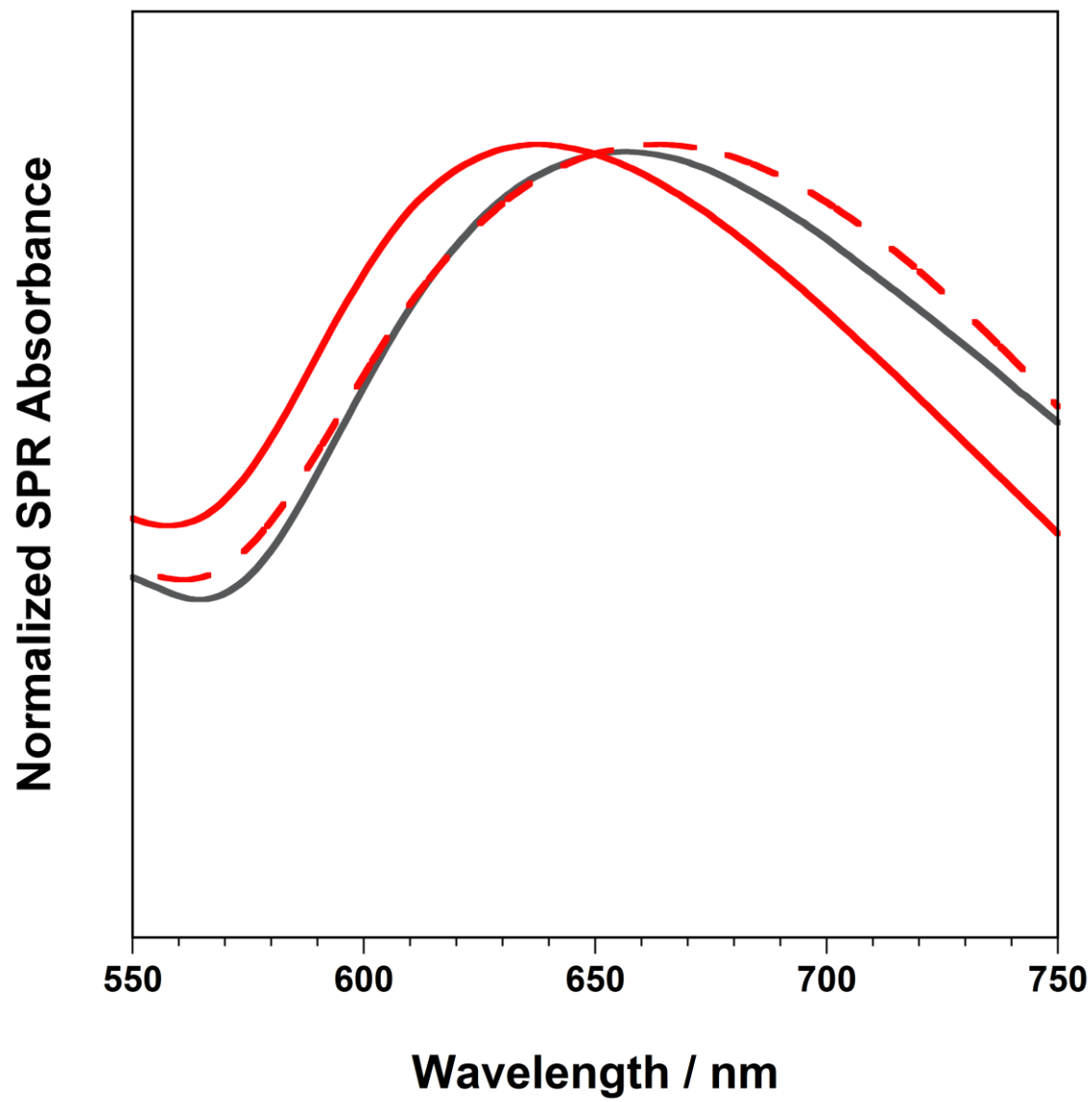
Figure 4



Mulder et al.

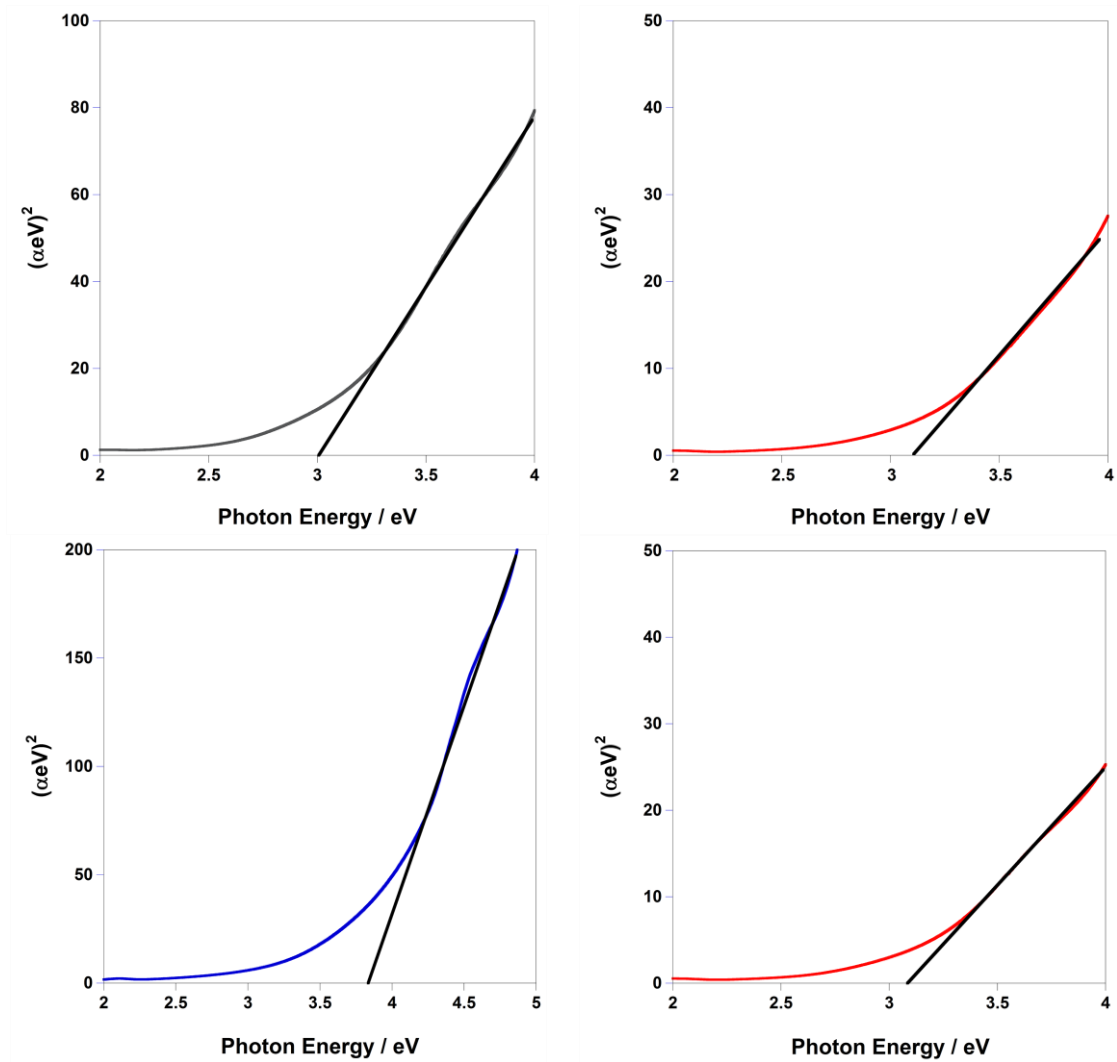
Figure 5





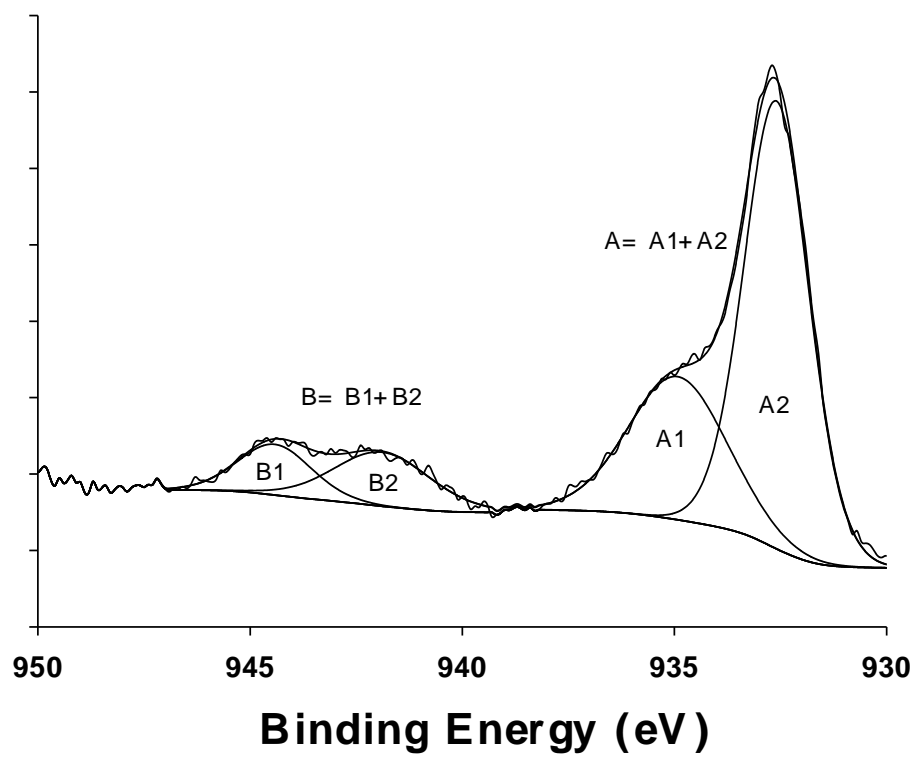
Mulder et al.

Figure 6



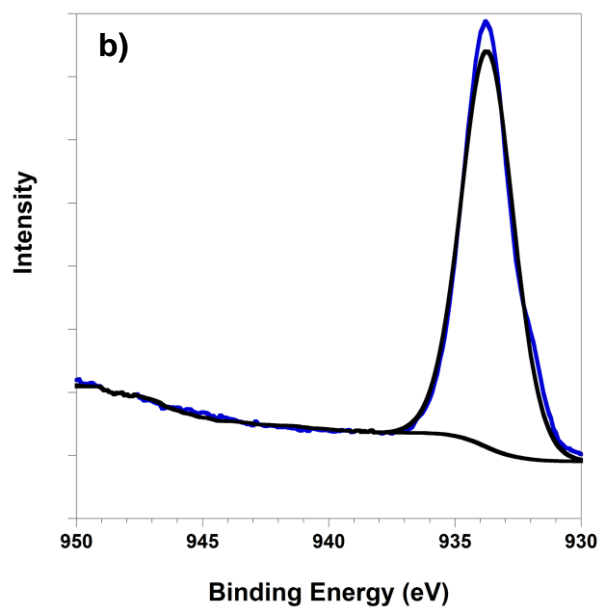
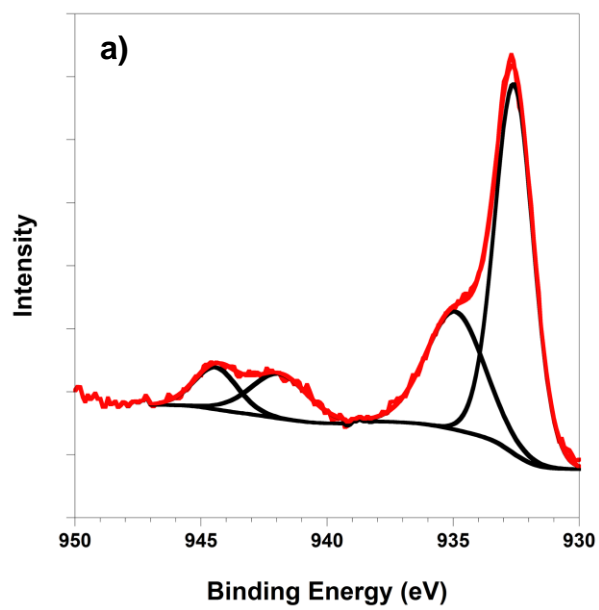
Mulder et al.

Figure 7



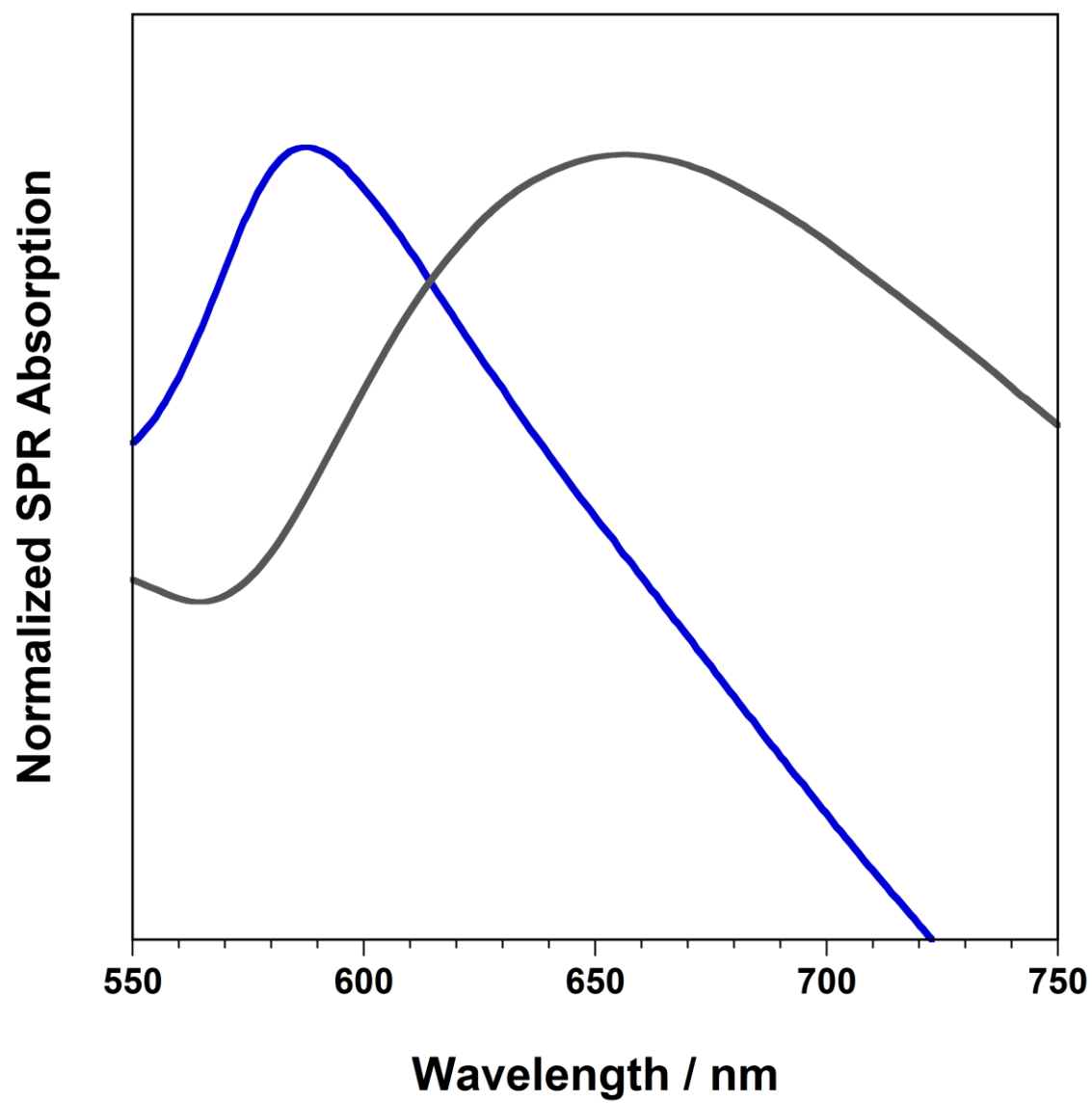
Mulder et al.

Figure 8



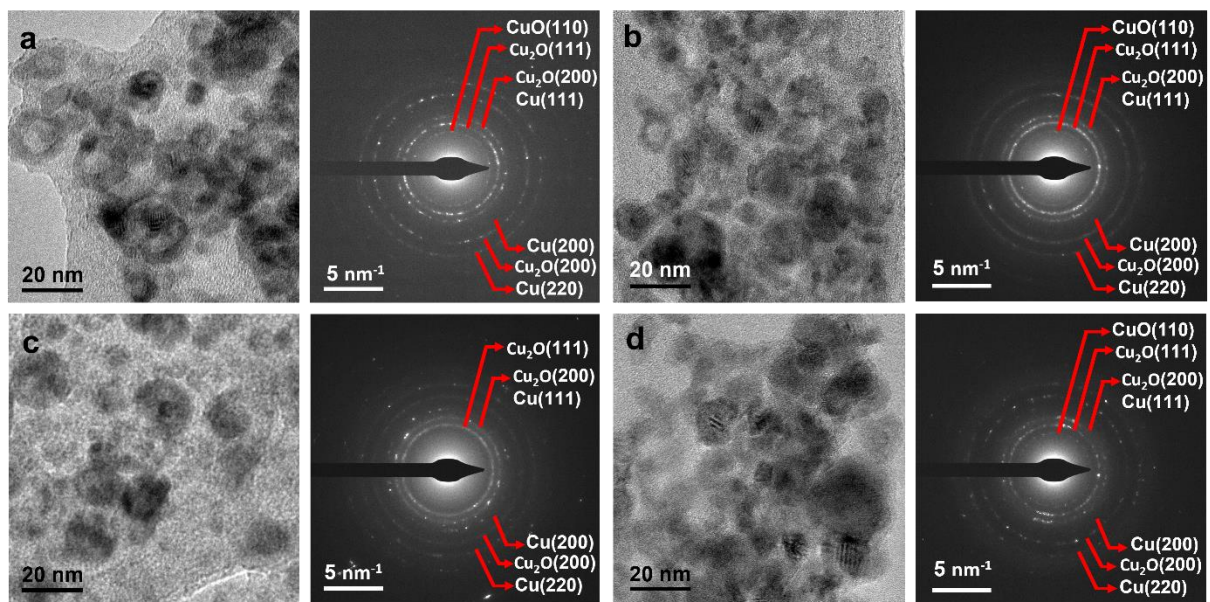
Mulder et al.

Figure 9



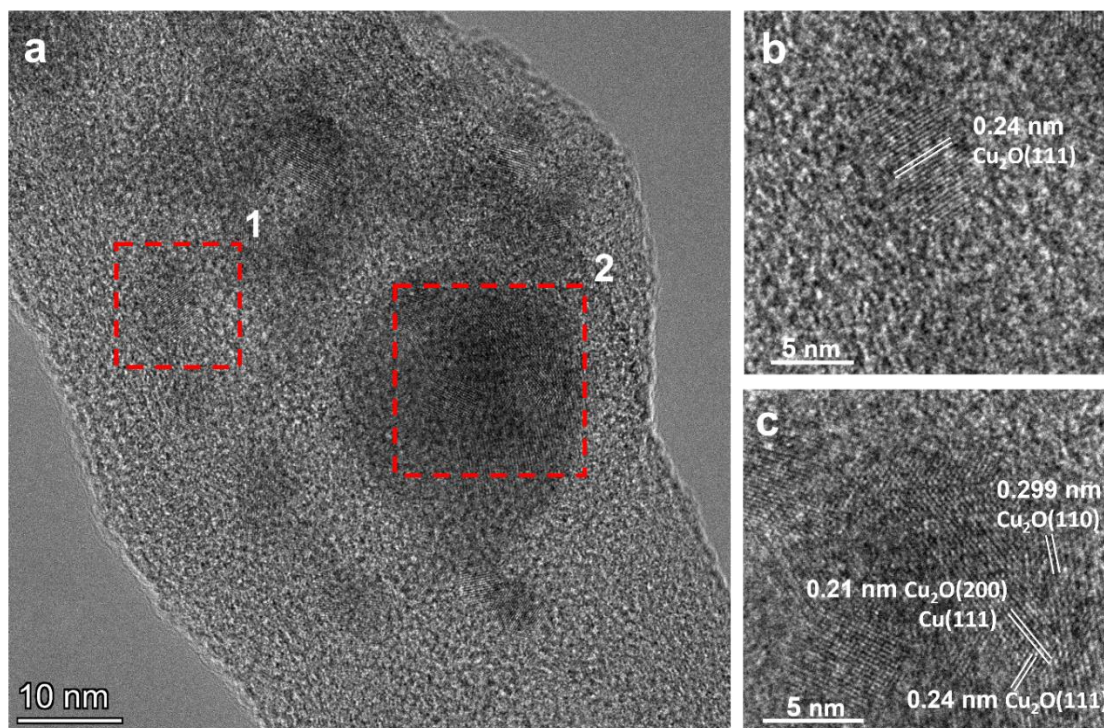
Mulder et al.

Figure 10



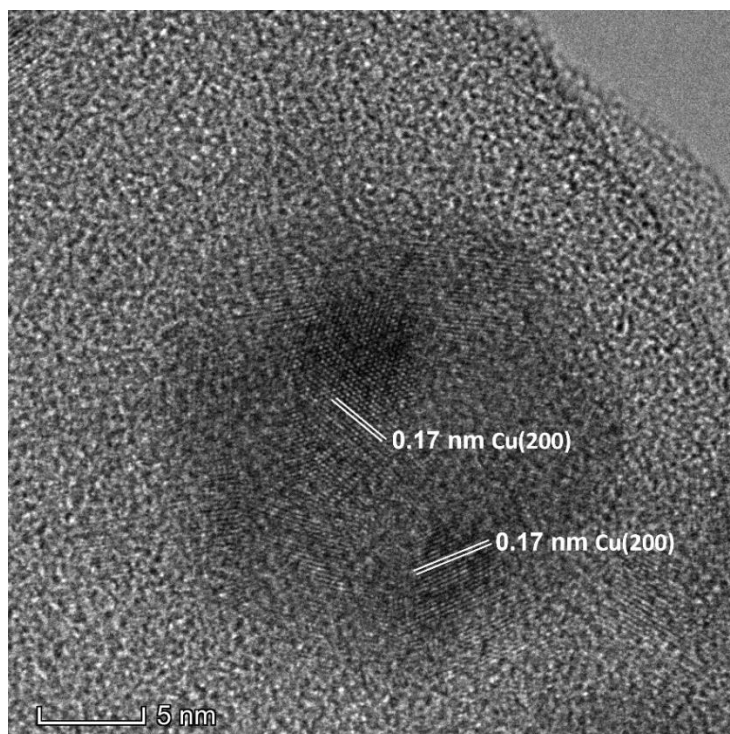
Mulder et al.

Figure 11



Mulder et al.

Figure 12

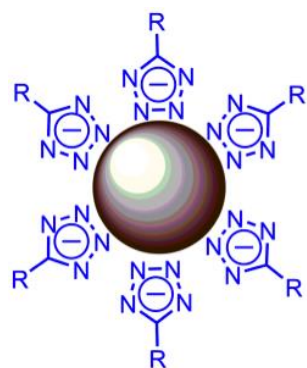


Mulder et al.

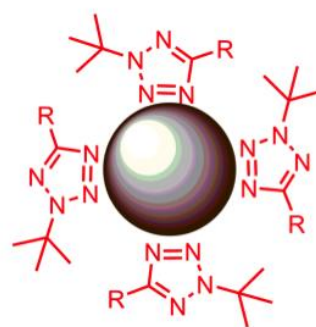
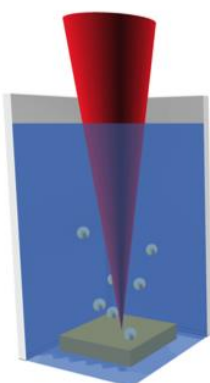
Figure 13



## TOC Graphic



SPR  $\lambda_{\max}$  = 590 nm



SPR  $\lambda_{\max}$  = 650 nm